



Review

# Zirconolite Polytypes and Murataite Polysomes in Matrices for the REE—Actinide Fraction of HLW

Sergey V. Yudintsev<sup>1</sup>, Maximilian S. Nickolsky<sup>1</sup> , Michael I. Ojovan<sup>1,\*</sup> , Olga I. Stefanovsky<sup>2</sup>, Boris S. Nikonov<sup>1</sup> and Amina S. Ulanova<sup>1</sup>

<sup>1</sup> Institute of Geology of Ore Deposits, Petrography, Mineralogy and Geochemistry, Russian Academy of Sciences (IGEM RAS), 119017 Moscow, Russia

<sup>2</sup> A.N. Frumkin Institute of Physical Chemistry and Electrochemistry, Russian Academy of Sciences (IPCE RAS), 119071 Moscow, Russia

\* Correspondence: m.i.ojovan@gmail.com

**Abstract:** Electron backscatter diffraction (EBSD) has been used for more than 30 years for analyzing the structure of minerals and artificial substances. In recent times, EBSD has been widely applied for investigation of irradiated nuclear fuel and matrices for the immobilization of radioactive waste. The combination of EBSD and scanning electron microscopy (SEM/EDS) methods allows researchers to obtain simultaneously data on a specimen's local composition and structure. The article discusses the abilities of SEM/EDS and EBSD techniques to identify zirconolite polytype modifications and members of the polysomatic murataite–pyrochlore series in polyphase ceramic matrices, with simulations of Pu (Th) and the REE-actinide fraction (Nd) of high-level radioactive waste.

**Keywords:** actinides; immobilisation; matrix; zirconolite; polytype; murataite; polysome; scanning electron microscopy; electron backscatter diffraction



**Citation:** Yudintsev, S.V.; Nickolsky, M.S.; Ojovan, M.I.; Stefanovsky, O.I.; Nikonov, B.S.; Ulanova, A.S. Zirconolite Polytypes and Murataite Polysomes in Matrices for the REE—Actinide Fraction of HLW. *Materials* **2022**, *15*, 6091. <https://doi.org/10.3390/ma15176091>

Academic Editors: Nabila Maloufi and Anastasios J. Tasiopoulos

Received: 8 July 2022

Accepted: 29 August 2022

Published: 2 September 2022

**Publisher's Note:** MDPI stays neutral with regard to jurisdictional claims in published maps and institutional affiliations.



**Copyright:** © 2022 by the authors. Licensee MDPI, Basel, Switzerland. This article is an open access article distributed under the terms and conditions of the Creative Commons Attribution (CC BY) license (<https://creativecommons.org/licenses/by/4.0/>).

## 1. Introduction

The development of sustainable nuclear power generation independent of uranium resources involves the reprocessing of spent nuclear fuel (SNF) with the recycling of uranium and actinides (Pu). The PUREX extraction process is industrially used for this, having initially been developed about 70 years ago in the USA to extract Pu and U for military purposes. Reprocessing a tonne of SNF generates 13–31 m<sup>3</sup> of liquid high-level radioactive waste (HLW). HLW can contain stable and radioactive isotopes of fission products (Cs, Ba, I, Sr, REE, Mo, Zr, Tc, Ru, Rh, Pd), residual U and Pu, minor actinides (Np, Am, Cm), corrosion products (Zr, Ni, Cr, Mn, Fe, Co, Al), and technological impurities (Na, Fe, Al, S). Liquid HLW poses an environmental hazard and must be converted into a stable form for placement in a deep underground repository. Since 1978, HLW has been immobilised in B–Si glass (France, UK, USA, Belgium, etc.), and since 1987, in Al–P glass (Russia). About 30 thousand tonnes of borosilicate and almost 7 thousand tonnes of aluminophosphate vitrified HLW have been produced up to now, and this process continues. Significant volumes of solid and liquid HLW are stored at radiochemical plants in the USA and Russia.

The weak point of glass is the low HLW loading, which is 3–5 wt.% for Al–P and 15–20 wt.% for B–Si matrices, as up to 1.8 t (0.6 m<sup>3</sup>) Al–P and 0.4 t (0.15 m<sup>3</sup>) B–Si glass matrix is produced on processing of 1 t of spent nuclear fuel. This reduces the efficiency of underground disposal, including the search for locations and the construction process, which require considerable time and resources. Other drawbacks of glass includes potential decrease in retaining properties due to crystallization, and on contact with water the formation of radioactive colloids migrating in the geological environment. The problems of HLW management can be more effectively solved by partitioning HLW into groups of elements with similar properties, for their immobilization in optimal matrices. One of these

groups is the fraction containing rare earth elements (REE) and minor actinides (MA) such as Am and Cm.

Russia is implementing a strategy of two-component nuclear power generation, with slow and fast neutron reactors operating in a closed nuclear fuel cycle [1]. This will reduce the need for uranium through the recycling of actinides, and will allow the extraction of useful stable and radioactive isotopes necessary for industry. The reprocessing of SNF will result in the generation of liquid high-level radioactive waste, so the development of methods for HLW optimal management is highly urgent. The greatest ecological concern is caused by long-lived actinides (Np, Pu, Am, Cm) and their daughter products [2–4], in particular,  $^{241}\text{Am}$  ( $T_{1/2} = 432$  years) decays to form  $^{237}\text{Np}$  with a half-life of 2.1 million years.

In the advanced nuclear fuel cycle, MAs are extracted for transmutation in fast reactors in homogeneous (Np) and heterogeneous (Am) modes [1,4–7]. There is a proposal to store Curium for 70 to 200 years, to decay into Pu and fabricate nuclear fuel. Depending on the degree of actinide extraction, the radioactive waste hazard will be equal to the value for uranium ore in 300, 500, or 10,000 years [1,2,4,7–9]. This concept is known as “radiative equivalence”. In a shorter time, about 100 years, radiological (oncological) equivalence between them will occur [10]. The application of this approach requires the creation of sophisticated technologies for processing SNF and extracting transplutonium elements (TPE) from HLW. Methods for partitioning REE, americium, and curium with similar properties, the separation of Am and Cm, fabrication of fuel with Np and Am, and its processing after irradiation in a fast reactor are still far from being implemented [11–14]. The timing of closing the nuclear fuel cycle, involving the partitioning of minor actinides (Np, Am, Cm), fuel fabrication, its irradiation in fast reactors, and subsequent reprocessing, has been shifted to 2050 [15], which is more than 30 years longer than previous estimates.

Comparison of the potential harm to human health from radioactive waste and U ore (radiative and oncological equivalence) is based on the assumption of their complete dissolution in groundwater. However, there are no real grounds for this, since uranium deposits with an age of many millions of years are known, representing reserves of hundreds of thousands of tonnes at concentrations of up to 20 wt.%. Reliably established reserves of uranium in these deposits are approach six million tones, and estimated resources are 7.5 million tonnes. The number of known U deposits exceeds 1800, the oldest of which are over 2 billion years old [16–18]. Since the solubilities of HLW and uranium ores in groundwater are very low, it makes no sense to compare their hazards. Environmental hazard assessment through the volume of water required to dissolve elements to a safe level has shown that Hg, Se, Pb, Cd, and As ores containing the first wt.% of these elements pose an even greater environmental threat [19–21]. Unlike radionuclides, which gradually decrease in quantity due to decay, the danger from these toxic elements does not decrease with time.

The main industrial minerals of U are uranium IV compounds; oxides (uraninite), phosphate (ningyoite), silicate (coffinite), and titanate (brannerite). Their ores are mined by underground leaching with the use of oxidizers, acidic, or alkaline solutions. The stability of U, Th, and REE minerals such as pyrochlore, perovskite, zircon, monazite, and britholite is even higher [22–25]. Zirconolite is highly stable in nature, with isotope systems that have been closed for hundreds of million years, making it possible to use zirconolite for age determination [26]. Therefore, alternatives to transmutation methods for management of HLW actinide fraction are based on the existence of geological settings in which actinide migration is practically absent. This approach consists of actinide immobilization in stable matrices and their placement at depths from hundreds of meters to 3–5 km in mined or borehole disposal facilities [19,27,28]. IAEA and NEA OECD reports have argued for the safety of SNF and HLW disposal [29,30]. Many countries, including Russia, are already implementing programs to select sites for the construction of HLW disposal facilities [4,31,32]. Methods have been developed for partitioning of PUREX nitric acid waste into fractions [2,11, 33–35]. The composition of the extraction mixture depends on the purpose of partitioning: For the extraction of Cs and Sr, CSEX and DDC processes are available; for REE and TPE—TRUOX,

UREX, TRPO, TODGA, DIAMEX; for extraction of all actinides—GANEX; UNEX is used for the Cs + Sr + REE + TPE group with subsequent separation into Cs–Sr and REE–TPE fractions. Some of these techniques have been tested on actual liquid HLW, confirming high levels of technological readiness—TRL6 or higher [36]. The presence of stable mineral-like phases and environments where actinide migration is absent or very low [19] proves the possibility of effectively handling actinide by incorporation into matrices and burial [37,38]. Localization of radionuclides will be ensured by engineering barriers and host-rocks' properties around a disposal facility (a mined repository or very deep borehole). Durable matrix (waste form) is the main engineering barrier of the HLW repository [39]. When choosing the matrix of the REE–MA fraction, it should be taken into account that lanthanides (La, Ce, Pr, Nd, Sm) dominate in its composition, and minor actinides (MA = Am, Cm) account for from 5 to 10 wt.% (Table 1) in the REE–MA mixture.

**Table 1.** (a) Composition (g/t) and (b) heat release (W/t) of SNF from light water reactors (LWR) depending on fuel burn and storage time [11].

Element	After 5 Years of Storage				After 30 Years of Storage			
	45 GW × d/t		60 GW × d/t		45 GW × d/t		60 GW × d/t	
	a	b	a	b	a	b	a	b
Gd, stable	150	0	310	0	180	0	346	0
Eu	190	60	260	90	170	8	230	12
Sm, stable	1060	0	1370	0	1120	0	1430	0
Pm	63	21	62	21	0	0	0	0
Ce	3210	10	4230	10	3210	0	4220	0
Pr	1540	114	2010	113	1540	0	2010	0
Nd, stable	5570	0	7310	0	5570	0	7310	0
La, stable	1670	0	2190	0	1670	0	2190	0
Σ REE	13,453	205	17,742	234	13,460	8	17,736	12
U	941,000	0.06	923,000	0.06	941,000	0.06	923,000	0.06
Pu	11,200	164	12,600	283	10,200	138	11,500	236
Np	570	0.01	780	0.02	570	0.01	780	0.02
Am	510	47	740	58	1380	146	1780	178
Cm	33	88	113	292	14	34	50	112
Am + Cm (MA) <sup>3+</sup>	543	135	853	350	1394	180	1830	290
REE/(REE + MA),%	96.2	60.3	95.4	40.1	90.6	4.3	90.7	4.0

REE, rare earth elements.

## 2. Requirements (Selection Criteria) for High-Level Waste Immobilization Matrices

The search for matrices for HLW fractions has been ongoing for several decades, and a number of criteria have been proposed [40]: (1) High waste loading (at least 20–35 wt.%) in order to minimize the volume and to maximize effective use of the repository; (2) simplicity, cost-effectiveness, and feasibility of manufacture; (3) resistance to radiation to exclude phase transformations over time, which reduce the stability of matrices; (4) corrosion resistance in water to prevent leaching of radionuclides, and their removal into the environment and the biosphere. A more detailed list is provided by references [41–43]: (1) High waste loading (up to 35 wt.%) to reduce waste volume in the geological repository. (2) Possibility of production under realizable conditions, using proven methods, minimizing the harmful effects on workers and reducing capital costs. (3) High resistance to radiation, including transmutation (transition into other elements), the effect of  $\alpha$ -particles and recoil nuclei on the matrix, and the effect of radiation from the decay of fission products. (4) Flexibility, low sensitivity to changes in HLW composition, and the ability to include a mixture of radionuclides and other elements without formation of phases that degrade the properties of the matrix. (5) Stability in groundwater under disposal conditions, to reduce the leaching of long-lived actinide radionuclides and fission products. (6) Existence of natural analogues; testing of waste forms for time scales of thousands of years or more is not possible, but

the presence of minerals with an age of hundreds of millions of years makes it possible to predict the behavior of the HLW matrix in a geological repository.

A similar set of criteria [44] takes into account the waste content in the matrix, the reality of industrial production, exclusion of a fission chain reaction, resistance to radiation, non-proliferation of fissile materials, and stability in underground waters. For actinide matrices, it is also necessary to exclude the possibility of spontaneous fission, for which it is proposed to introduce neutron absorbers REE or Hf in the matrix.

For vitrified HLW used in Russia, properties have been determined including uniformity of composition, maximal heat release, thermal and radiation resistance, leachability, mechanical strength, and thermo-physical parameters [45,46]. The main method of radionuclide release from the repository and their entry into the biosphere is leaching from the matrix by groundwater, therefore stability of solutions is among their most important properties.

Matrix properties can be divided into three groups: physical, chemical, and technological. The first group of parameters includes density, porosity, coefficients of linear and volume expansion, heat capacity, melting point (glass transition temperature for vitreous matrices), and thermal conductivity [45,47]. The chemical parameters consist of resistance to leaching, structural changes during radioactive decay, as well as crystal chemical parameters including the solubility of elements in glass, the capacity of the crystal structure, the valence and coordination of REE and actinide cations, the cation–oxygen distance, the strength of the cation field, and the type of elemental bonding. Technological properties are understood as physical properties that determine the possibility of obtaining a matrix on an industrial scale, for example, the melting temperature and the reaction rate during solid-state sintering. The physical and chemical parameters of matrices and their influence on the long-term behavior of solidified radioactive waste are summarized in Table 2.

**Table 2.** Physical (nos. 1–12) and chemical (13–14) parameters of radionuclide matrices.

Nos.	Characteristic and Its Unit	Influence on the Properties of the HLW Matrix
1	Density, g/cm <sup>3</sup>	Amount of waste in the matrix and its volume
2	Poisson's ratio	Mechanical strength and block stability
3	Young's modulus, MPa	Mechanical strength and block stability
4	Compressive strength, MPa	Mechanical strength and block stability
5	Shear modulus, MPa	Mechanical strength and block stability
6	Radiation resistance, Gray	Exposure behavior on the decay of radionuclides
7	Thermal resistance, °C	Thermal behavior on the decay of radionuclides
8	Melting point, °C	Affects the matrix manufacturing technology
9	Glass transition temperature, °C	Thermal stability of glasses to crystallization
10	Expansion coefficient, °C <sup>-1</sup>	Thermal behavior on the decay of radionuclides
11	Specific thermal conductivity, W m <sup>-1</sup> K <sup>-1</sup>	Heating during the decay of radionuclides
12	Heat capacity, J g <sup>-1</sup> K <sup>-1</sup>	Heating during the decay of radionuclides
13	Solubility of waste, wt.%	Affects the amount of waste in the matrix
14	Leaching rates, g m <sup>-2</sup> day <sup>-1</sup>	Ability of the matrix to retain radionuclides

Simulators (REEs) are typically used when studying MA (Am, Cm) matrices. Most often, Nd is used [48,49] due to the close ionic radii of Nd<sup>3+</sup>, Am<sup>3+</sup>, and Cm<sup>3+</sup> in the same coordination [50,51] and the predominance of Nd in the REE-MA fraction (Table 1). Cerium can be used to simulate Pu, because it has oxidation states of 3+ and 4+ appropriate to Pu [44]. Isovalent and heterovalent isomorphism and exchanges involving vacancies play important roles in the immobilization of actinides in crystal structures [51–57]. The charge and size of cations affect the loading of matrices with waste, affecting solubility in glass [58] and isomorphic capacity of the crystalline phases. When the content of elements is higher than this value, phases of REE and MA are formed, for example, REE and MA oxides, which is undesirable because of their higher solubility in water than that of target matrix phases.

The phenomena of morphotropy, polytypism and polysomatism are widely manifested in the HLW matrices. Titanates and zirconates of the REE<sub>2</sub>(Zr/Ti)<sub>2</sub>O<sub>7</sub> composition are



characterized by morphotropic transitions. As the ion radius decreases from light to heavy REE (from  $\text{La}^{3+}$  to  $\text{Yb}^{3+}$  and  $\text{Y}^{3+}$ ), the phase structure changes from perovskite to pyrochlore in titanates and from pyrochlore to fluorite in zirconates. For the former, the boundary lies between  $\text{Nd}^{3+}$  and  $\text{Sm}^{3+}$ , for the latter it passes between  $\text{Sm}^{3+}$  and  $\text{Gd}^{3+}$ . A dramatic change in the structure of the phases, by five orders of magnitude, affected the rate of REE leaching of titanate phases [59,60], from  $1.5 \times 10^{-4} \text{ g}/(\text{m}^2 \times \text{day})$  for  $\text{Yb}_2\text{Ti}_2\text{O}_7$  (pyrochlore) to  $10 \text{ g}/(\text{m}^2 \times \text{day})$  in  $\text{La}_2\text{Ti}_2\text{O}_7$  (perovskite-like structure), but was found to have almost no effect on REE zirconates with pyrochlore or fluorite structures. Variations in the composition of pyrochlore  $\text{REE}^{3+}_2\text{B}^{4+}_2\text{O}_7$  ( $\text{B} = \text{Ti, Sn, Zr}$ ) also influence initial rate of REE leaching: from  $0.393 \text{ mmol}/(\text{m}^2 \times \text{day})$  for  $\text{La}_2\text{Sn}_2\text{O}_7$  to  $0.007 \text{ mmol}/(\text{m}^2 \times \text{day})$  for  $\text{Yb}_2\text{Zr}_2\text{O}_7$  [61]. Morphotropic transitions can also affect the resistance of matrices to irradiation; decreasing for  $\text{REEPO}_4$  [62] when the structure of zircon (heavy REE phosphates) changed to monazite (light REE). Among REE titanates of  $(\text{REE})_2\text{TiO}_5$  composition, cubic phases are more resistant to radiation than compounds with hexagonal and rhombic structures [25].

Polytypism is associated with the existence of structures that differ only in their layer sequences, for example, when they are shifted or rotated with an increase in the period of the structure. The cell parameter in the direction of layer packing is a multiple of the distance between adjacent layers. Polytypes are usually designated by a combination of a number to show the number of layers in an elementary cell and a letter that indicates the symmetry [63]; cubic (C), hexagonal (H), rhombohedral (R), trigonal (T), orthorhombic (O), or monoclinic (M). The most widely known example of this phenomenon in the actinide matrices (waste forms) is due to five polytypes of zirconolite (2M, 4M, 3O, 3T, and 6T).

The concept of polysomatism implies the presence of different blocks or modules in the structure of a compound [64,65]. The end members of polysomatic series have modules of the same type and composition. The structures of intermediate members (polysomes) consist of blocks of the end-member structures. They are present in HLW matrices in the form of murataite–pyrochlore polysomatic series [66–68], where pyrochlore and murataite 3C are the end members, and murataites 5C, 7C, and 8C are intermediate members (Figure 1) [68].

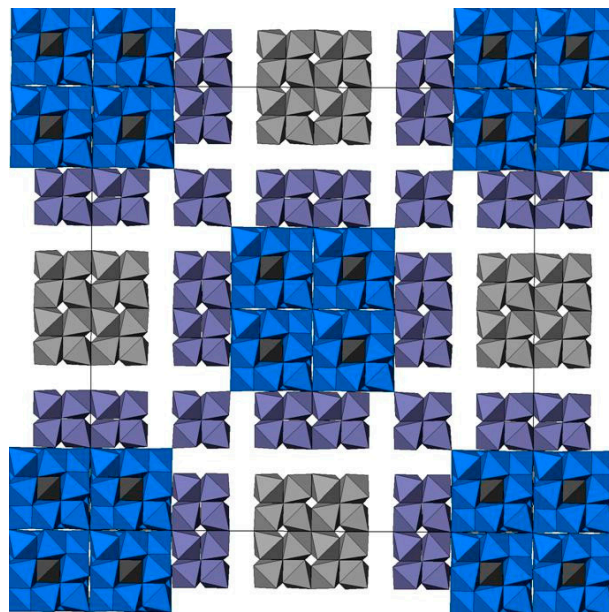


**Figure 1.** Combination of murataite 3C (blue)–pyrochlore (gray) modules and pyrochlore-type blocks (violet) in the structure of murataite 8C polysome.

According to their different compositions, polytypes and polysomes are discernable in color in the backscattered electron (BSE) images of a scanning electron microscope,

but establishing their structure and assigning them to a specific polytype (polysome) is a difficult task. Methods based on X-ray phase analysis and transmission electron microscopy have been used for this goal [66–68], not always possible in view of the small quantities of these phases in the samples. The aim of this article is to demonstrate the possibilities of electron backscatter diffraction (EBSD) in determining zirconolite polytypes and murataite polysomes in actinide matrices. First, we consider general information about the structural features of these groups of compounds.

### 3. Zirconolite and Murataite as Matrices for the Immobilization of Actinides

The choice of actinide matrix is largely determined by crystal–chemical parameters. At high temperatures, the most common oxidation states of actinides are  $\text{Pu}^{3+/4+}$ ,  $(\text{Am}, \text{Cm})^{3+}$  and  $\text{Np}^{4+}$  [69]. REE elements of the REE-MA fraction (MA = Am, Cm) exist as trivalent ions, Ce can be partially in the form of  $\text{Ce}^{4+}$ . To simulate actinides in matrices, lanthanides are used, and Ce, Th or U are introduced instead of Pu [47,70,71]. Due to close ionic radii [50],  $\text{Ce}^{3+}$  simulates  $\text{Pu}^{3+}$ , while  $\text{Nd}^{3+}$  and  $\text{Eu}^{3+}$  simulate  $\text{Cm}^{3+}$  and  $\text{Am}^{3+}$ . Monovalent  $\text{Th}^{4+}$  and  $\text{Hf}^{4+}$  are sometimes used to replace Np and Pu. Particular attention is paid here to studies using Nd, Sm, or La, which dominate among the REE fission products of SNF and in the composition of the REE-MA fraction of HLW. The average ionic radius of the REE-MA fraction is 1.11 Å, the same as for  $\text{Nd}^{3+}$ , larger than that of  $\text{Sm}^{3+}$  (1.08 Å), but smaller than that of  $\text{La}^{3+}$  (1.16 Å). Therefore, Nd is the best simulant of the REE-MA fraction when studying the structure and waste loading of the matrices, the distribution of elements between phases, stability in water, and their main physical properties; density, heat capacity, thermal conductivity, and mechanical durability, which weakly depend on whether the simulant element is radioactive.

For the immobilization of actinide containing nuclear waste, crystalline zirconolite and glass-crystalline materials with zirconolite have been proposed. They may be obtained by all known methods—sintering at atmospheric or elevated pressures, melting and crystallization, high-speed pulsed electric current sintering, and self-propagating high-temperature synthesis [57,72–92]. Zirconolite is stable in various natural conditions [22,24,25,75]; natural zirconolite is a rare mineral of terrestrial and lunar igneous rocks, and metasomatites. In nature, zirconolites from different localities have been found to contain  $\text{UO}_2$ ,  $\text{ThO}_2$ , or  $\text{REE}_2\text{O}_3$  reaching 24, 22, or 32 wt%, respectively [23,25,93]. Due to the high content of U and Th, zirconolite is often amorphous; this occurs at irradiation doses above  $5 \times 10^{18}$   $\alpha$ -decays/g [22]. In Figure 2, three minerals can be distinguished by composition: Zirconolite, monoclinic (polytype 2M), polymignite, orthorhombic (3O), zirkelite, hexagonal (3T) [94].

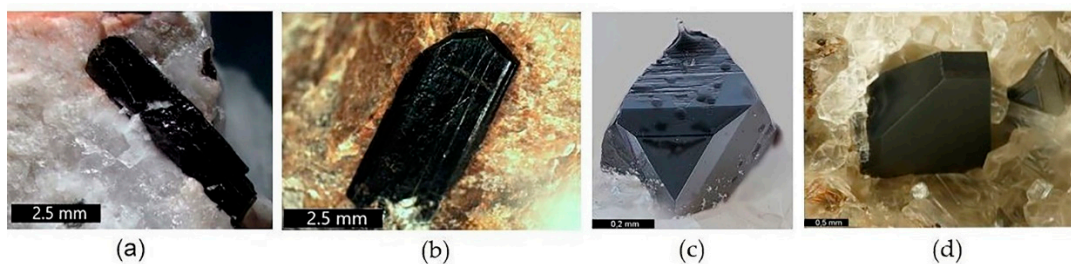


**Figure 2.** Natural zirconolites: (a,b) 3O (Vestfold og Telemark, Norway); and (c,d) 3T (Eifel Volcanic Fields, Germany; Fogo Volcano, Portugal).

The above noted classification was approved by the Commission on New Minerals of the International Mineralogical Association [95]; hence, polymignite and zirkelite are no longer used. The 2M polytype is common in carbonatites, while the 3O and 3T polytypes are common in volcanics and metasomatites [96,97] with a content of  $\text{REE}^{3+}$ , Th, Fe, and Nb.

Artificial zirconolite was observed for the first time in Synroc polyphase ceramics [72], an alternative to B–Si glass for HLW immobilization. In the first version, Synroc A, the  $(\text{Zr}, \text{Ca}, \text{Ti})\text{O}_2$  oxide initially was determined, but X-ray microanalysis found that its formula

corresponded to  $\text{CaZrTi}_2\text{O}_7$  with an admixture of Al for charge balance when the Ca/Zr ratio varied. This allowed attribution of the phase found to an artificial analog of the mineral zirconolite, which later was confirmed by the X-ray diffraction data. In the all Synroc-type ceramics (B, C, D, E, F), zirconolite is the main host for actinides and REE [28,51,72,73,98]. It forms five polytypes—2M, 4M, 3O, 3T, and 6T, the figure is the number of layers of  $\text{TiO}_6$  octahedra, the letter is the symmetry of the lattice. The structure of the 2M polytype consists of trigonal and hexagonal rings of Ti-O octahedra, some of the Ti atoms are surrounded by 5  $\text{O}^{2-}$  anions. These correspond to three positions of Ti atoms: Ti(1) and Ti(3) with a coordination number (cn) equal to VI (octahedrons), and Ti(2) with  $\text{cn} = \text{V}$  (bipyramids). The unit cell of zirconolite contains eight Ti(1) atoms, and four each of Ti(3) and Ti(2) atoms.  $\text{Ca}^{2+}$  ( $\text{cn} = \text{VIII}$ ) and  $\text{Zr}^{4+}$  ( $\text{cn} = \text{VII}$ ) are located between two networks of  $\text{TiO}_6$  octahedra. One structural module is formed by a pair of layers of  $\text{TiO}_6$  octahedra with interlayer cations. Its rotation through an angle multiple of  $120^\circ$  forms a cell of zirconolites 3T and 3O. With a change in the stacking sequence of Ca/Zr and Ti–O layers, other polytypes arise, and the structure of zirconolite 4M is a four-layer package of sheets of zirconolite 2M and pyrochlore (Figure 3).

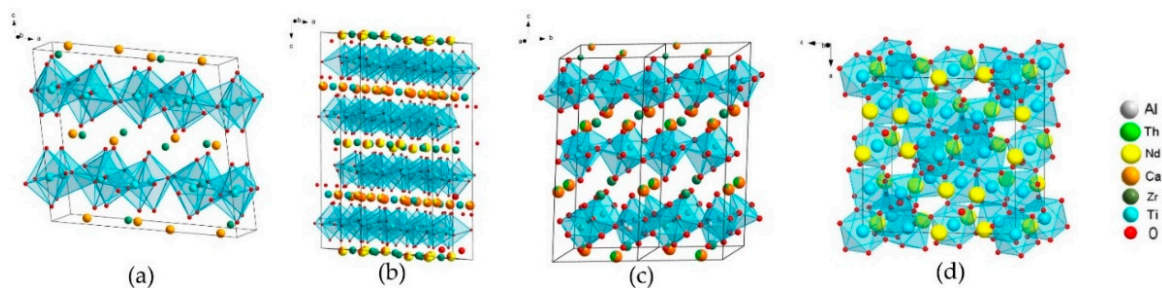


**Figure 3.** Structure of zirconolite polytypes (a) 2M, (b) 4M, (c) 3T, (d) pyrochlore  $\text{Nd}_2(\text{Ti,Zr})_2\text{O}_7$ .

The result is a doubling of the cell parameter along the  $c$  axis with preservation of monoclinic symmetry [99]. Variations in composition of the 2M phase are described by the formula  $\text{CaZr}_x\text{Ti}_{3-x}\text{O}_7$ , “ $x$ ” = 0.83–1.33. The replacement of Zr by Hf retains the 2M structure in  $\text{CaHfTi}_2\text{O}_7$  and  $\text{Ca}_{1-x}\text{Nd}_x\text{HfTi}_{2-x}\text{Al}_x\text{O}_7$  ( $x = 0.01, 0.2$ ) [100], which is due to the closeness of ionic radii of  $\text{Zr}^{4+}$  (0.78 Å) and  $\text{Hf}^{4+}$  (0.76 Å) ( $\text{cn} = \text{VII}$ ).

Among the first works to note the effect of zirconolite composition on its structure were articles [51,74,101,102]. A description of all five zirconolite polytypes known so far is given in [103]. Their formation depends on the type of substitutions, charge and radius of cations, temperature, and oxidizing conditions [104]. Polytypes 2M and 4M are monoclinic (sp. gr.  $C2/c$ ), 3O is orthorhombic ( $Acam$ ), and 3T and 6T are hexagonal ( $P3_121$ ). The most common polytypes in actinide matrices are 2M and 4M [104], less common are 3O [82] and 3T [70,105], there are no data for the 6T polytype. For phases of composition  $(\text{Ca}_{1-x}\text{Pu}_x)\text{Zr}(\text{Ti}_{2-2x}\text{Fe}_{2x})\text{O}_7$  ( $x = 0.1\text{--}0.7$ ), the 2M polytype is stable up to “ $x$ ” = 0.3, and 3T appears at “ $x$ ” = 0.3 and 0.4. Replacing Pu with Ce increases the field of stability of the 2M polytype. Zirconolite 3T is often formed using thorium as a simulator. A reducing medium (5%  $\text{H}_2/\text{N}_2$ ) is favorable for the formation of 3T zirconolite  $\text{CaZr}_{1-x}\text{Th}_x\text{Ti}_2\text{O}_7$  at  $x \geq 0.20$  [104],  $\text{Ca}_{0.8}\text{Ti}_{1.35}\text{Zr}_{1.3}\text{Th}_{0.15}\text{Al}_{0.4}\text{O}_7$  crystallizes in the same 3T type [106]. Fine intergrowth of 2M and 3T polytypes was established in glass ceramics obtained in the  $\text{SiO}_2\text{--Al}_2\text{O}_3\text{--CaO--ZrO}_2\text{--TiO}_2\text{--ThO}_2$  system [80].

$\text{CaZr}_{1-x}(\text{Ce/U/Th/Pu})_{4+x}\text{Ti}_2\text{O}_7$  ( $x = 0.1\text{--}0.6$ ) phases are represented by zirconolite 2M, 4M and/or pyrochlore (Table 3), and their structures shown in Figure 3, with data from [104].

**Table 3.** Phases in samples of bulk composition  $\text{CaZr}_{1-x}(\text{Ce}/\text{U}/\text{Th}/\text{Pu})_{4+x}\text{Ti}_2\text{O}_7$  at “x” from 0.1 to 0.6.

Cation	x = 0.10	x = 0.20	x = 0.30	x = 0.40	x = 0.50	x = 0.60
Ce <sup>4+</sup>	2M	2M + 4M	2M + 4M	2M + 4M	2M + 4M + P	4M + P
U <sup>4+</sup>	2M	2M + 4M	2M + 4M	4M + P	4M + P	4M + P
Th <sup>4+</sup>	2M + P	2M + P	2M + P	2M + P	2M + P	P
Pu <sup>4+</sup>	2M	2M + 4M	2M + 4M	4M + P	4M + P	P

2M, 4M—zirconolite polytypes, P—pyrochlore.

Information about zirconolite polytypes in glass ceramics is controversial. On the one hand [88,89], in B–Si glass ceramics, with an increase in the contents of CeO<sub>2</sub> and Nd<sub>2</sub>O<sub>3</sub> up to 15 wt%, transition of 2M polytype into 4M was observed. However, when studying glass ceramics with  $\text{Ca}_{1-x}\text{Zr}_{1-x}\text{Nd}_{2x}\text{Ti}_2\text{O}_7$ ,  $\text{Ca}_{1-x}\text{Nd}_x\text{ZrTi}_{2-x}\text{Al}_x\text{O}_7$ , and  $\text{CaZr}_{1-x}\text{Ce}_x\text{Ti}_2\text{O}_7$  ( $x = 0\text{--}0.5$ ) phases, no transition of the 2M to 4M polytype was observed, in contrast to ceramics of the same composition [107]. In glass ceramics with REE and actinides, the 2M polytype is more stable due to the limited solubility of tri- and, especially, tetra-valent cations in the original glass [58,108] and low distribution coefficients of Nd<sup>3+</sup>, Ce<sup>3+</sup>, Th<sup>4+</sup> between zirconolite and glass [80,109,110] during crystallization in the glass ceramic.

Compositions of natural and artificial zirconolite can be affected by substitutions [23,51,75], the main ones being  $(\text{Ce},\text{An})^{4+} \rightarrow \text{Zr}^{4+}$ ;  $2(\text{Ln},\text{An})^{3+} \rightarrow \text{Ca}^{2+} + \text{Zr}^{4+}$ ;  $(\text{Ln},\text{An})^{3+} + (\text{Al},\text{Fe})^{3+} \rightarrow \text{Ca}^{2+} + \text{Ti}^{4+}$ ; and more rarely:  $\text{An}^{4+} + (\text{Fe},\text{Co})^{2+} \rightarrow \text{Ca}^{2+} + \text{Ti}^{4+}$ ;  $(\text{Ce},\text{An}^{4+}) + 2(\text{Al},\text{Fe},\text{Cr})^{3+} \rightarrow \text{Ca}^{2+} + 2\text{Ti}^{4+}$  (Ln are lanthanides, An are actinides). The replacement of 2M zirconolite by more complex 4M, 3O, or 3T polytypes has been observed with an increase in the concentration of tri- (La, Ce, Nd, Dy, Y, Am, Cm) and tetravalent ions (Ce, U, Np, Pu), replacing Ca<sup>2+</sup> and Zr<sup>4+</sup> [44,104,111–113]. An increase in the content of Nd<sup>3+</sup> or (Ce/U/Th/Pu)<sup>4+</sup> in the samples resulted in the zirconolite sequence structure 2M–3T–4M–pyrochlore [100,104].

In many early [28,72,73,98,114,115] and more recent [92,116,117] studies of matrices, the zirconolite polytype was not specified. There are several explanations for this and the first is that the similarity of properties [80] may make it unnecessary to identify the exact zirconolite polytype. There is no clear evidence that structural features somehow affect the resistance of zirconolite to radiation or corrosion in water [44]. It can only be argued that the polytypes have different capacities with respect to the actinide and REE-actinide fractions, i.e., maximum value for 4M, minimum for 2M, and intermediate for zirconolite 3O or 3T. With an actinide and REE content of up to 0.20–0.25 atoms, the zirconolite polytype 2M is stable [118,119]. The boundary between 2M and 4M polytypes for the  $\text{Ca}_{1-x}\text{Zr}_{1-x}\text{Sm}_{2x}\text{Ti}_2\text{O}_7$  solid solution passes at  $x = 0.35$  [120].

Artificial zirconolite with REE and Pu is stable in alkaline and acidic solutions up to 500 °C at 50 MPa, even after amorphization of the crystalline lattice [23,77,83,121–124].

Murataite was first discovered in the Synroc matrix from defense waste obtained by sintering [125]. In the sample from the HLW simulator [66,67,126], obtained by melting and crystallization, it was formed from the melt last, growing on zirconolite grains (Figure 4) [127].

Such a close relationship between these two phases is due to the affinity of the structures both derived from the fluorite-type lattice. Murataite is this optimal host phase for tetravalent actinides (Th, U, Np, Pu); in this case it dominates in the matrix (Figure 5) [66,67].

In the nature, murataite has been found in only two locations, making it significantly rarer than zirconolite. Unlike zirconolite, murataite contains neither U nor Th, and of the rare earth elements contains only Y.

With an increase in the content of trivalent REE in the sample, perovskite-like phase has been observed, a less stable phase at elevated water solution temperatures, especially above 100 °C [128]. Synthetic murataites occur as phases 3C, 5C, 7C, and 8C (the number is the multiplicity of the cell parameter relative to the fluorite cell, C is the cubic symmetry of the lattice). They constitute the polysomatic series murataite 3C—pyrochlore [68,129–131].



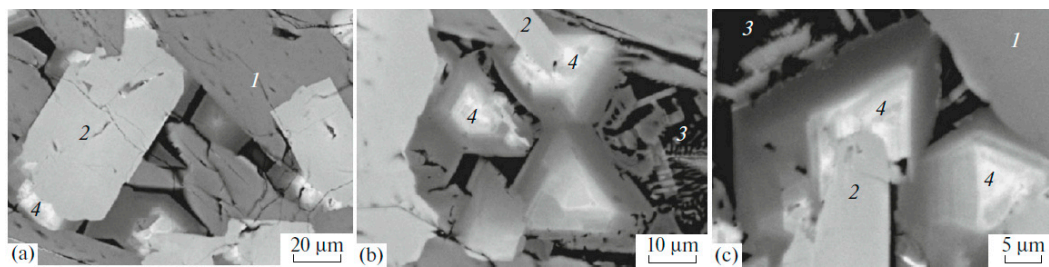


**Figure 4.** SEM images of the melted Synroc-type ceramic with model nuclear wastes: (1) hollandite, (2) zirconolite, (3) rutile and glass, (4) zoned murataite crystals overgrown on the zirconolite grains. (a) general view; (b,c) details with murataite–zirconolite intergrowths.

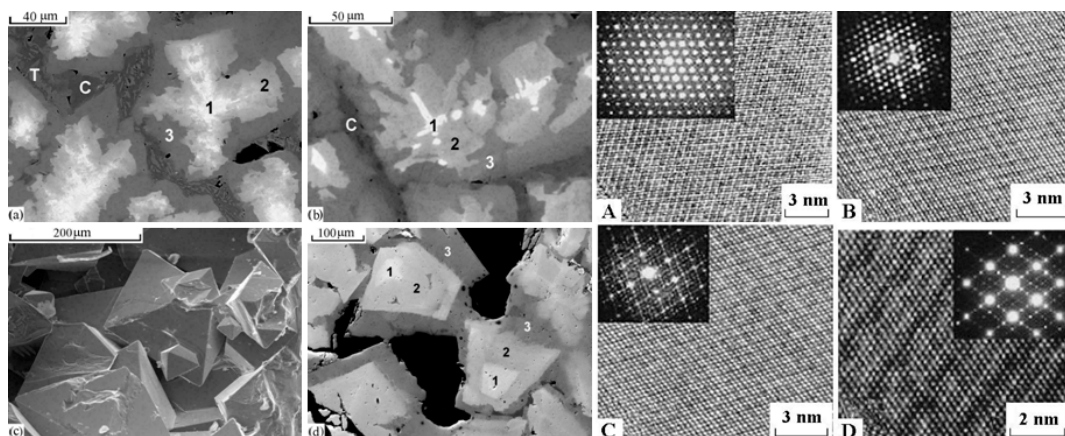


**Figure 5.** Left: SEM images of ceramics with 10% (a)  $\text{UO}_2$ , (b)  $\text{PuO}_2$ , (c,d)  $\text{ThO}_2$ . (1) murataite 5C, (2) murataite 8C, (3) murataite 3C, (C) crichtonite, (T) pyrophanite; pores are black. Right: HRTEM micrographs of (A) pyrochlore, murataite (B) 3C, (C) 5C, (D) 8C taken with a high-resolution transmission electron microscope. Inserts: SAED patterns. Lines are atomic layers.

Murataites 5C and 8C are the most common in samples, whereas 3C is less common and 7C is very rare. All of them crystallize in the sp. gr. F-43m, so their X-ray diffraction patterns are similar. In melted ceramics, murataite forms zoned crystals with pyrochlore or murataite 5C at the center, and murataite 8C or 3C towards the edges (Figure 5). In samples obtained by sintering, murataite 5C and murataite 8C formed separate grains [132]. The pyrochlore module is responsible for actinide content, and the murataite block is responsible for corrosion products (Fe, Al, Mn). Although the concentrations of actinides decrease in the order pyrochlore–murataite 5C–8C–3C, while Fe and Al increase, the assignment of the phase to a specific polysome only by its composition may be incorrect.

Elucidation of the polytype (polysome) of phase requires examination by X-ray phase analysis with attention to weak reflections from a certain range of angles, or in a transmission electron microscope [82,100,103]. This problem is often complicated by the multiphase composition of matrices and the presence of several phases with similar structures—zirconolite, pyrochlore, and murataite. For simultaneous study of the composition and structure of phases, a combination of scanning electron microscopy (SEM) and electron backscatter diffraction (EBSD) can be applied [133,134]. The possibilities of this approach will later be shown using the example of samples containing zirconolite and murataite, but first we must present brief information about the electron backscatter diffraction method.

#### 4. Characteristics of Electron Backscatter Diffraction Method

The EBSD method is based on the scattering of an incident electron beam in a sample, with the formation of a “point” source of electrons that coherently scatter and create a diffraction pattern which is recorded by a CCD detector. It presents a set of intersecting

light stripes bounded by dark lines, called Kikuchi bands after the name of the scientist who first described this effect [135]. The method has been used in scanning electron microscopy since the 1970s [136,137]. To obtain EBSD patterns, the sample (Figure 6) is tilted at an angle of  $70^\circ$  which allows an increase in the proportion of electrons leaving the sample.

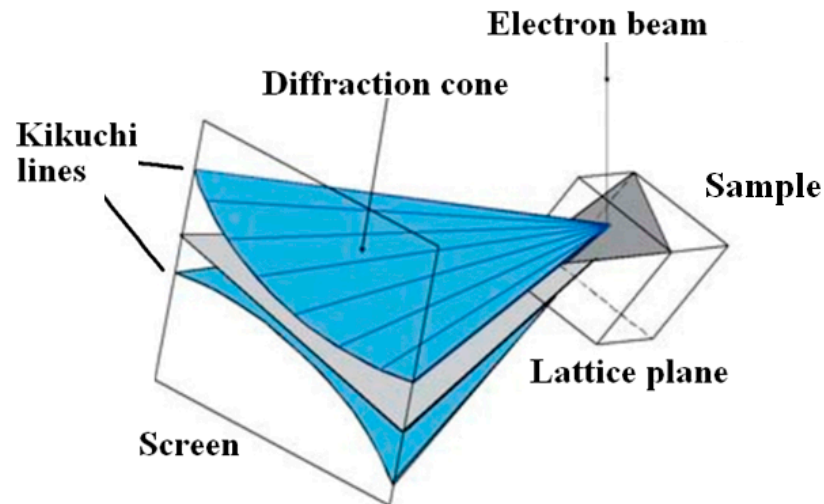


**Figure 6.** Obtaining of Kikuchi Lines in a scanning electron microscope by the EBSD method.

When the Bragg diffraction condition is met, two cone-shaped electron beams are formed for each family of planes, and fixed on the screen. The digital camera is positioned horizontally so that the screen is closer to the sample for a wider capture of the diffraction pattern. The width of the Kikuchi bands is proportional to the doubled Bragg reflection angle ( $2\theta$ ) and inversely proportional to the interplanar spacing ( $d_{hkl}$ ). The angles between the Kikuchi bands are related to the angles of the crystallographic planes, and the points of their intersection correspond to the projections of the zone axes. EBSD pattern analysis makes it possible to determine the size and orientation of grains and their boundaries, to reveal the stress–strain state, the process of recrystallization, and the structure of phases.

In recent years, EBSD has been used in nuclear power engineering to analyze fuel based on  $\text{UO}_2$  or U-Mo and its claddings (Zr-Nb alloys) before and after irradiation in a reactor [138], and also the effect of annealing on the structure of materials [139,140]. In certain works [141,142] it is used as an auxiliary technique for studying the structure and phase composition of nuclear waste matrices. However, the possibilities of this method are much wider [133,134]. The purpose of this work is to study the structure of zirconolite and murataite in matrices with actinide simulators (Th, Nd) obtained by melting in air at  $1500^\circ\text{C}$  in glassy carbon crucibles.

## 5. EBSD Study of Zirconolite Polytypes and Murataite Polysomes

### 5.1. Zirconolite—Murataite Matrix with Thorium (Sample “Th”)

The composition of the sample was wt%: 50  $\text{TiO}_2$ , 10  $\text{CaO}$ , 10  $\text{MnO}$ , 5  $\text{Al}_2\text{O}_3$ , 5  $\text{Fe}_2\text{O}_3$ , 10  $\text{ZrO}_2$ , 10  $\text{ThO}_2$ . Powder diffraction pattern showed reflections of murataite (major phase) and zirconolite (Figure 7a). According to SEM/EDS data (Figure 7b), the main volume was occupied by gray grains surrounded by a dark mass. In the center of the grains are light elongated zirconolite crystals. The phase compositions are shown in Table 4; average values (wt%) as follows: 4.2  $\text{Al}_2\text{O}_3$ , 10.5  $\text{CaO}$ , 49.8  $\text{TiO}_2$ , 8.7  $\text{MnO}$ , 2.8  $\text{Fe}_2\text{O}_3$ , 11.4  $\text{ZrO}_2$ , 12.5  $\text{ThO}_2$  (gray, murataite-1); and 8.8  $\text{Al}_2\text{O}_3$ , 9.5  $\text{CaO}$ , 54.7  $\text{TiO}_2$ , 11.0  $\text{MnO}$ , 7.3  $\text{Fe}_2\text{O}_3$ , 2.1  $\text{ZrO}_2$ , 6.6  $\text{ThO}_2$  (dark, murataite-2). The difference in the color of the grains of phases 1 and 2 was caused by different contents of Th, Zr, Fe, and Al. Composition of zirconolite, wt%: 1.8  $\text{Al}_2\text{O}_3$ , 10.2  $\text{CaO}$ , 39.7  $\text{TiO}_2$ , 4.0  $\text{MnO}$ , 1.4  $\text{Fe}_2\text{O}_3$ , 29.5  $\text{ZrO}_2$ , 13.3  $\text{ThO}_2$ .

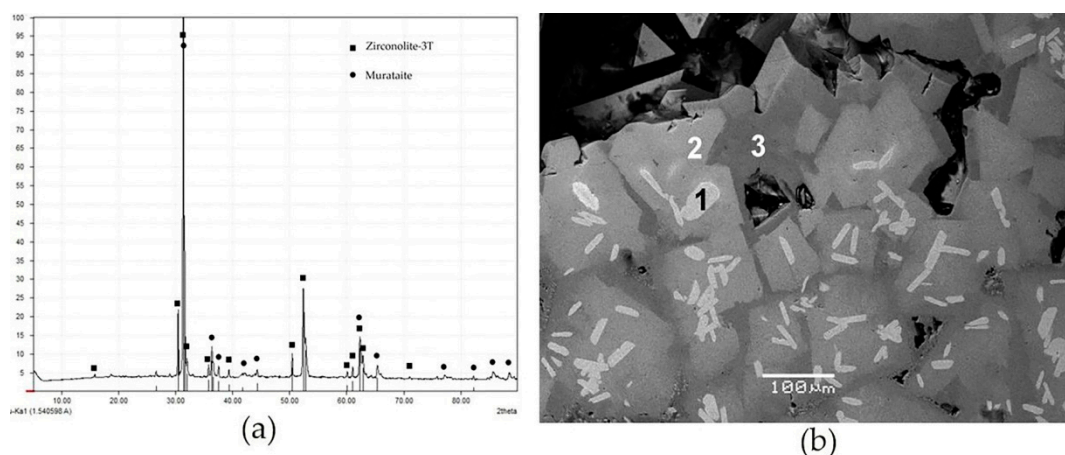


**Figure 7.** (a) X-ray powder diffraction pattern and (b) SEM image of sample “Th”: 1—zirconolite, 2—murataite-1, 3—murataite-2, blackp—ores. Markers on the XRD pattern show the peak positions only. The high-resolution diffraction pattern is given in Appendix A.

**Table 4.** Phase compositions of sample “Th” ( $\Sigma = 100$  wt.%, SEM/EDS data).

Phase	Al	Ca	Ti	Mn	Fe	Zr	Th	O
Zirconolite	0.8	7.5	23.6	3.0	1.1	23.0	10.8	30.2
Zirconolite	0.9	7.1	24.6	3.5	1.3	19.6	12.8	30.2
Zirconolite	1.3	7.2	23.3	2.7	0.6	23.0	11.6	30.3
Murataite-1 <sup>1</sup>	2.5	7.6	30.9	6.9	2.1	7.8	9.4	32.8
Murataite-1	2.0	7.8	29.2	6.8	1.9	10.0	10.2	32.1
Murataite-1	1.9	7.4	28.8	6.6	1.9	9.1	12.7	31.6
Murataite-2	4.6	7.0	33.1	8.2	4.5	2.6	5.2	34.8
Murataite-2	4.8	7.1	31.8	7.8	4.4	3.0	6.6	34.5
Murataite-2	4.7	6.4	32.8	8.7	4.8	2.0	5.9	34.7

<sup>1</sup> Murataite 1 and 2—from the central and marginal parts of the zoned grains, respectively.

According to SEM/EDS analysis data, the phases were formed from the melt in the sequence zirconolite—murataite-1—murataite-2. The presence of two phases of murataite makes it important to identify their polysome and zirconolite polytypes. In the region of angles  $2\theta \sim 30^\circ$ , the peaks of zirconolite and murataite overlapped, and the low amount of zirconolite in the sample,  $\sim 10$  vol.%, complicated the problem. The EBSD method served as the optimal technique for solving it. The EBSD pattern was obtained for one of the sections (Figure 8) for this purpose, with processing and indexing of the bands carried out automatically. Analysis of the EBSD patterns of zirconolite allowed its 3T polytype to be determined, and both varieties of murataite were found to be 8C polysomes. According to SEM/EDS data, the zirconolite formula was  $\text{Ca}_{0.67}\text{Th}_{0.19}\text{Ti}_{1.84}\text{Zr}_{0.89}\text{Fe}_{0.07}\text{Mn}_{0.21}\text{Al}_{0.13}\text{O}_7$ . The formulas for murataite calculated on  $823 \text{ O}^{2-}$  [68] corresponded to  $\text{Ca}_{76.52}\text{Th}_{19.4}\text{Ti}_{254.73}\text{Zr}_{37.86}\text{Fe}_{14.54}\text{Mn}_{50.35}\text{Al}_{33.55}\text{O}_{823}$  for the central part (m-1) and  $\text{Ca}_{65.04}\text{Th}_{9.53}\text{Ti}_{259.29}\text{Zr}_{6.31}\text{Fe}_{34.68}\text{Mn}_{58.8}\text{Al}_{65.04}\text{O}_{823}$  for marginal parts (m-2) of the zoned grains.

### 5.2. Pyrochlore—Zirconolite Ceramic with Neodymium (Sample “Nd”)

As mentioned earlier,  $\text{Nd}^{3+}$  serves as an analogue of  $\text{Am}^{3+}$  and  $\text{Cm}^{3+}$  as well as of the REE-MA fraction as a whole. Therefore, when searching for a matrix for the REE-MA fraction, neodymium titanates and zirconates are of great interest. In the  $\text{NdO}_{1.5}$ — $\text{TiO}_2$ — $\text{ZrO}_2$  system, the following phases are formed [143]:  $\text{Nd}_2(\text{Ti,Zr})_2\text{O}_7$  (pyrochlore structure),  $\text{Nd}_2\text{Ti}_2\text{O}_7$  and  $\text{Nd}_2\text{Ti}_4\text{O}_{11}$  (perovskite-like structures),  $\text{Nd}_2\text{TiO}_5$ , and  $\text{Nd}_4\text{Ti}_9\text{O}_{24}$ . Note that no information is given about the appearance of zirconolite in this system. These matrices were previously obtained by sintering or melting—crystallization [48,144–146].



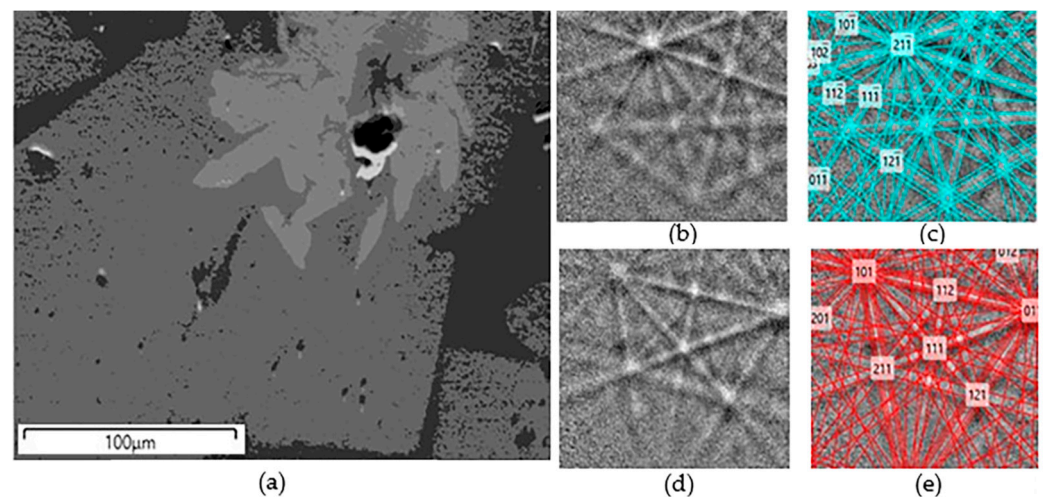


**Figure 8.** (a) SEM image of the analysed area, light—zirconolite, gray and dark-gray—murataite, and EBSD patterns of (b,c) zirconolite and (d,e) murataite, (b,d) before and (c,e) after indexing.

The sample “Nd” studied by the EBSD method was prepared by melting for 0.5 h at 1500 °C in a glassy carbon crucible. Its composition as well as spots of other samples (S3–S5, S8) are shown in Figure 9a. For ease of plotting,  $\text{NdO}_{1.5}$ ,  $\text{TiO}_2$ , and  $\text{ZrO}_2$  are located at the vertices of the triangular diagram [143]. The composition, mol % 35  $\text{NdO}_{1.5}$ , 13  $\text{Nd}_2\text{O}_3$ , 52  $\text{ZrO}_2$  (or 21  $\text{Nd}_2\text{O}_3$ , 16  $\text{ZrO}_2$ , 63  $\text{TiO}_2$ ) corresponds to the association of pyrochlore  $\text{Nd}_2(\text{Zr,Ti})_2\text{O}_7$  and srilankite  $\text{ZrTiO}_4$ . Nevertheless, the X-ray diffraction pattern showed pyrochlore reflections and weak rutile peaks (Figure 9b). The SEM/EDS study established its composition of two neodymium titanium-zirconates as well as rutile (Figure 9, Table 5).

**Table 5.** Phase compositions averaged over three to five determinations ( $c$ —center,  $e$ —edge), wt%, and zirconolite formulae calculated for four cations (without  $\text{Ti}^{3+}$ ) or four cations and  $7\text{O}^{2-}$  (accounting for  $\text{Ti}^{3+}$ ).

Phase	Ti	Zr	Nd	O	Only $\text{Ti}^{4+}$ Suggested	Formulae of Zirconolite with Both $\text{Ti}^{3+}$ and $\text{Ti}^{4+}$
Pyrochlore	16.5	13.1	46.9	23.5	$\text{Nd}_{1.35}\text{Zr}_{0.59}\text{Ti}_{1.41}\text{O}_{6.02}$	$\text{Nd}_{1.35}\text{Zr}_{0.59}\text{Ti}_{1.41}\text{O}_{6.02}$
Zirconolite $c$	21.5	14.6	38.1	25.8	$\text{Nd}_{1.22}\text{Zr}_{0.74}\text{Ti}_{2.04}\text{O}_{7.40}$	$\text{Nd}_{1.22}\text{Zr}_{0.74}\text{Ti}^{4+}_{1.26}\text{Ti}^{3+}_{0.78}\text{O}_7$
Zirconolite $e$	23.5	11.8	38.5	26.2	$\text{Nd}_{1.20}\text{Zr}_{0.60}\text{Ti}_{2.20}\text{O}_{7.40}$	$\text{Nd}_{1.20}\text{Zr}_{0.60}\text{Ti}^{4+}_{1.40}\text{Ti}^{3+}_{0.80}\text{O}_7$
Rutile	46.8	7.0	10.7	35.5	$\text{Ti}_{0.86}\text{Zr}_{0.07}\text{Nd}_{0.07}\text{O}_{1.97}$	$\text{Ti}_{0.86}\text{Zr}_{0.07}\text{Nd}_{0.07}\text{O}_{1.97}$

The grains of the light-colored phase had sections with shapes close to isometric. Taking into account the XRD data and the composition, it was determined as pyrochlore. The second phase (gray) composed elongated crystals surrounding light grains. Between them were black areas composed of rutile, with small inclusions of pyrochlore. The color of elongated crystals varied from gray to dark gray, reflecting the compositions (Table 5). The difference between isometric light grains and elongated gray grains was manifested in the content of  $\text{TiO}_2$  and, to a lesser extent,  $\text{ZrO}_2$  and  $\text{Nd}_2\text{O}_3$ . High, non-typical content of  $\text{Nd}_2\text{O}_3$  in rutile is connected with the capture of fine grains of the light phase (pyrochlore) inside the aggregates of rutile grains. When calculating the phase formulas for two atoms  $\text{Zr} + \text{Ti}$  (pyrochlore) and four atoms  $\text{Nd} + \text{Zr} + \text{Ti}$  (zirconolite), a low value of the  $\text{O}^{2-}$  number in the pyrochlore formula and its high values in the zirconolite formula were obtained. Compared to the ideal formula  $\text{A}_2\text{B}_2\text{O}_6\text{O}'$ , there was a deficiency of cations in the A position and an absence of the  $\text{O}'$  anion in the formula of the pyrochlore. Defective pyrochlores were found in the samples S3–S5, S8 (Figure 9), obtained by melting–crystallization [144,147,148]. The difference between the formula of zirconolite and the ideal one with seven  $\text{O}^{2-}$  lies in the reduction of part of the  $\text{Ti}^{4+}$  to  $\text{Ti}^{3+}$  during the reaction of the melt within the carbon



crucible:  $\text{Ti}^{4+}\text{O}_2 + \text{C} = \text{Ti}^{3+} + \text{CO}_2$ . Taking this into account, a formula was calculated closer to the real values for zirconolite with the number of cations equal to four and seven  $\text{O}^{2-}$  anions (Table 5).

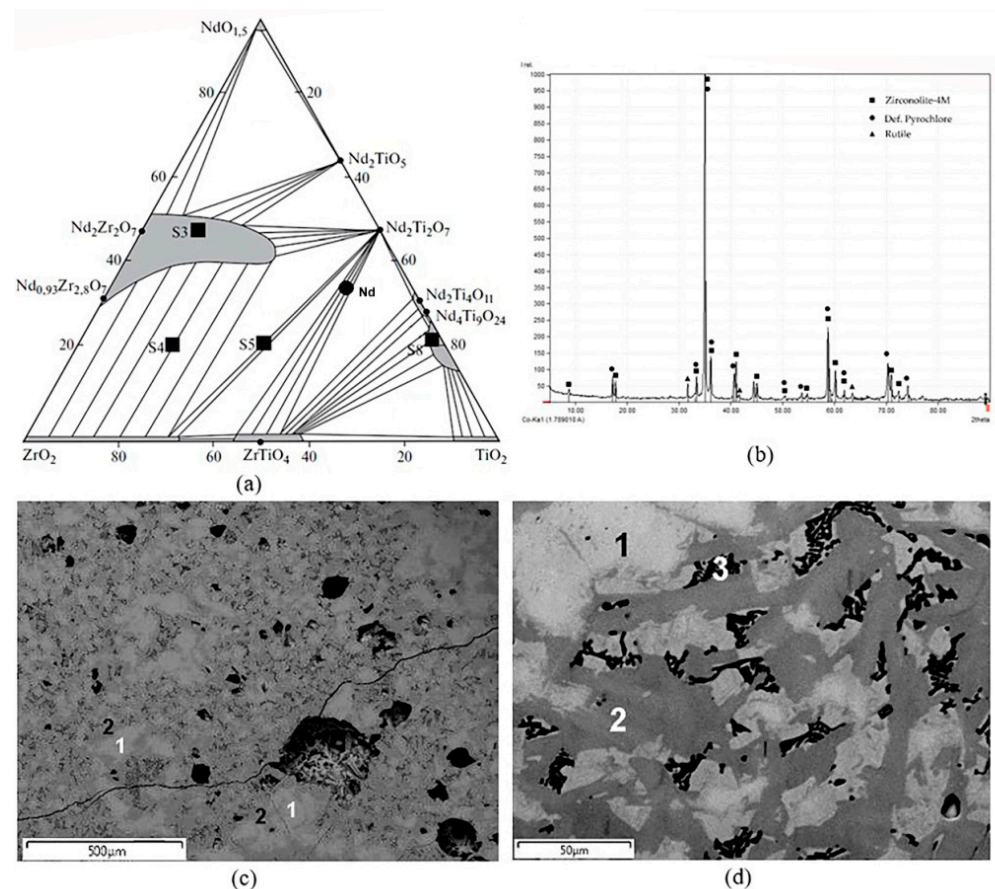


**Figure 9.** (a) Position of the “Nd” sample, (b) its X-ray diffraction pattern, and (c,d) SEM/EDS images: 1—pyrochlore, 2—zirconolite, 3—rutile (black) with fine pyrochlore inclusions. The scale bars on the SEM images are (c) 500 and (d) 50  $\mu\text{m}$ . Markers on the XRD pattern show the peak positions only. The high-resolution diffraction pattern is given in Appendix B.

To determine the structure of the light (pyrochlore) and gray (zirconolite) phases, the sample was studied by EBSD. As a result, the pyrochlore structure for the light phase was confirmed, and the best match for the EBSD patterns for the gray phase was found to be the 4M zirconolite polytype (Figure 10). These structural features contradict the data [143] suggesting the absence of zirconolite in the  $\text{NdO}_{1.5}\text{—TiO}_2\text{—ZrO}_2$  system. In most of the samples studied by us, obtained in this system by sintering or melting [148], for example, S3–S5, S8 (Figure 9), zirconolite was not found, and their phase composition mainly corresponded to the phase diagram (Table 6). Zirconolite was previously found only in two samples [48,144]. Their actual and calculated compositions (Table 7) differed in the presence of  $\text{Al}_2\text{O}_3$  (impurity in the charge) and  $\text{ZrO}_2$  (Zr to initiate melting). As a result, in addition to monoclinic or rhombic Nd titanates, they were found to contain 10–30 vol.% of zirconolite (Figure 11).

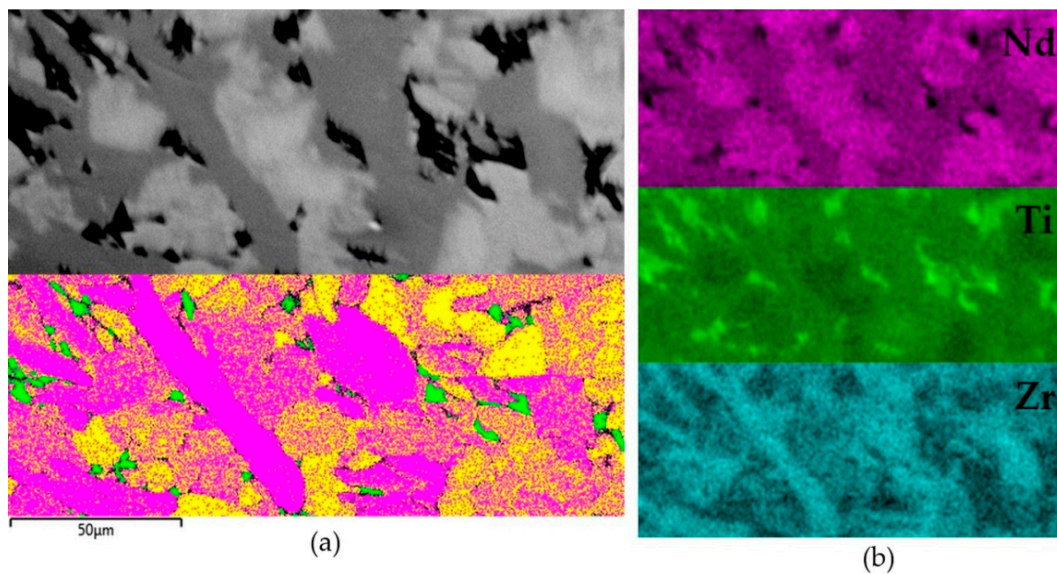


**Figure 10.** The structure of sample “Nd”: (a) top—BSE image (light—pyrochlore, gray—zirconolite, dark—rutile), bottom—EBSD map (yellow—pyrochlore, violet—zirconolite-4M, green—rutile); (b) distribution of Nd, Ti, Zr within the sample.

**Table 6.** Chemical (mol.%) and phase compositions of samples: (a) expected [143]; (b) actual phases present according to XRD and SEM/EDS studies [148].

Sample	NdO <sub>1.5</sub>	ZrO <sub>2</sub>	TiO <sub>2</sub>	Phase Composition: Expected (a) and Real (b)
S3	50	37.5	12.5	P <sup>a</sup> / P <sup>b</sup>
S4	20	60	20	P—B/B—O—B
S5	20	40	40	B—TN—1/B—P—TZ
S8	23	0.02	75	TN—2/TN—2—R <sup>1</sup>

<sup>1</sup> P—pyrochlore Nd<sub>2-x</sub>(Ti, Zr)<sub>2</sub>O<sub>7-1.5x</sub>, B—monoclinic baddeleyite ZrO<sub>2</sub>, O—cubic oxide (Zr, Nd)O<sub>2-x</sub>, TN-1—Nd<sub>2</sub>Ti<sub>2</sub>O<sub>7</sub>, TZ—ZrTiO<sub>4</sub>, TN-2—Nd<sub>4</sub>Ti<sub>9</sub>O<sub>24</sub>, R—rutile (Ti, Zr)O<sub>2</sub>.

**Table 7.** (1) Calculated and (2) actual compositions of the MT and RT samples and their phases—monoclinic (m) and orthorhombic (o) Nd titanates and zirconolite polytype (z-3O).

Oxide/Ion	MT				RT			
	1	2	m	z-3O	1	2	o	z-3O
Al <sub>2</sub> O <sub>3</sub>	-	0.8	n.d. <sup>1</sup>	3.1	-	2.2	n.d.	6.7
TiO <sub>2</sub>	32.9	28.5	31.4	33.1	52.5	48.5	50.5	37.6
ZrO <sub>2</sub>	-	6.2	0.8	25.2	-	5.0	1.6	19.6
Nd <sub>2</sub> O <sub>3</sub>	67.1	64.5	67.8	38.5	47.5	44.3	47.9	36.1
Al <sup>3+</sup>	-	-	n.d.	0.27	-	-	n.d.	0.54
Ti <sup>4+</sup>	2.00	-	1.96	1.82	9.00	-	8.82	1.93
Zr <sup>4+</sup>	-	-	0.03	0.90	-	-	0.18	0.65
Nd <sup>3+</sup>	2.00	-	2.01	1.01	4.00	-	4.00	0.88
O <sup>2-</sup>	7.00	-	6.99	7.37	24.00	-	24.00	7.29

<sup>1</sup> n.d.—not detected. The target phases were monoclinic Nd<sub>2</sub>Ti<sub>2</sub>O<sub>7</sub> (sample MT) and orthorhombic Nd<sub>4</sub>Ti<sub>9</sub>O<sub>24</sub> (sample RT).

Another reason for zirconolite’s appearance in the MT and RT samples (as in the sample “Nd”) is related to the reduction of part of Ti<sup>4+</sup> to Ti<sup>3+</sup> with the exchange: Ca<sup>2+</sup> + Ti<sup>4+</sup> = Nd<sup>3+</sup> + (Al,Ti)<sup>3+</sup>. This explains the high O<sup>2-</sup> value (7.29 and 7.37) and the different atomic amounts of Nd<sup>3+</sup> and Al<sup>3+</sup> in the formulas (Table 7). The reduction of Ti was probably caused by the high temperature of synthesis and the introduction of Zr (met.).

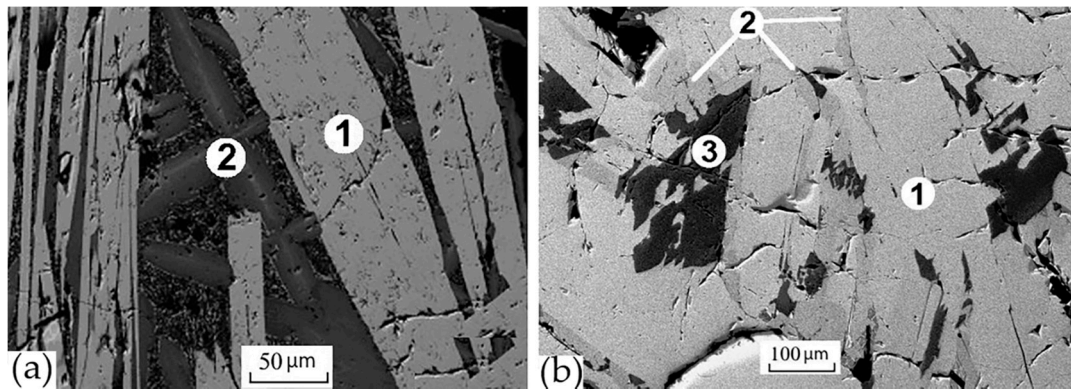


**Figure 11.** SEM images of the samples (a) MT: 1—monoclinic  $\text{Nd}_2\text{Ti}_2\text{O}_7$ , 2—zirconolite; (b) RT: 1—orthorhombic  $\text{Nd}_4\text{Ti}_9\text{O}_{24}$ , 2—zirconolite, 3—rutile.

## 6. On the Simulators of Actinides and REE-Actinide Fraction in Nuclear Waste Matrices

Structural data obtained for a sample with stable elements and natural actinides (Th, U) is relevant to matrices with real radionuclides only if the simulator (REE, U, Th) is chosen correctly. For fractions of trivalent minor actinides (MA–Am, Cm) and REE–MA,  $\text{Nd}^{3+}$  serves as an optimal simulator due to the proximity of ionic radii in the corresponding coordination [48,107]. Their compounds have the same structure, for example monoclinic perovskite-like for  $\text{Nd}_2\text{Ti}_2\text{O}_7$  and  $\text{Am}_2\text{Ti}_2\text{O}_7$  [149], whilst REE titanates with a radius smaller than that of  $\text{Nd}^{3+}$  form a cubic pyrochlore structure. Hence, the use of  $\text{Dy}^{3+}$  as an simulator of  $\text{Am}^{3+}$  and other trivalent actinides is not quite correct [150]. A more complex picture can be observed when plutonium is replaced: Ce has often been used for this purpose due to the close ion radii in the  $\text{Ce}^{3+}$ – $\text{Pu}^{3+}$  and  $\text{Ce}^{4+}$ – $\text{Pu}^{4+}$  pairs. However, the stability fields of these ions do not coincide ( $\text{Ce}^{4+}$  is more easily reduced to  $\text{Ce}^{3+}$ , the stability of  $\text{Pu}^{4+}$  is higher), and therefore no complete analogy is maintained between them. To simulate Pu,  $\text{Ce}^{3+}$  is recommended in a reducing environment, while  $\text{Th}^{4+}$  is recommended in an oxidizing one [104]. Sometimes  $^{\text{VIII}}\text{Hf}^{4+}$  ( $r = 0.83 \text{ \AA}$ ) can serve as a  $\text{Pu}^{4+}$  simulator, but due to difference in ionic radii, this choice cannot be considered a good option.

## 7. Conclusions

Morphotropic transitions in actinide matrices composed of phosphates, titanates, and zirconates of rare earth elements resulted in a variety of structures of host phases. They also exhibited polytypism (zirconolite) and polysomatism (pyrochlore–murataite series). One of the important requirements for the matrix is a high waste content; therefore, the 4M, 3T, and 3O zirconolite polytypes and the 5C and 8C murataite polysomes are of interest. Their diagnostics by X-ray phase analysis can often be difficult due to the multiphase structures of matrices, with the presence of several phases at once structurally derived from the fluorite lattice (pyrochlore, zirconolite, murataite, cubic Zr oxide).

The structural types of phases in samples with simulators of actinide and REE-actinide fractions (Th, Nd) were determined using electron backscatter diffraction. The sample with Th contained zirconolite-3T of composition  $\text{Ca}_{0.67}\text{Th}_{0.19}\text{Ti}_{1.84}\text{Zr}_{0.89}\text{Fe}_{0.07}\text{Mn}_{0.21}\text{Al}_{0.13}\text{O}_7$  and two phases—polysomes of murataite 8C:  $\text{Ca}_{76.52}\text{Th}_{19.4}\text{Ti}_{254.73}\text{Zr}_{37.86}\text{Fe}_{14.54}\text{Mn}_{50.35}\text{Al}_{33.55}\text{O}_{823}$  and  $\text{Ca}_{65.04}\text{Th}_{9.53}\text{Ti}_{259.29}\text{Zr}_{6.31}\text{Fe}_{34.68}\text{Mn}_{58.8}\text{Al}_{65.04}\text{O}_{823}$ . The zirconolite in the sample with Nd was represented by the 4M polytype, pyrochlore is also present. The stability fields of zirconolite polytypes depend on the size of the cations that replace the main elements ( $\text{Ca}^{2+}$ ,  $\text{Ti}^{4+}$ , and  $\text{Zr}^{4+}$ ). The replacement of  $\text{Zr}^{4+}$  by  $(\text{Ce}, \text{U}, \text{Pu})^{4+}$  caused the transformation of the 2M polytype into 4M. Replacements of  $\text{Ca}^{2+}$ – $\text{Zr}^{4+}$  and  $\text{Ca}^{2+}$ – $\text{Ti}^{4+}$  with  $\text{Pu}^{3+/4+}$ ,  $\text{REE}^{3+}$ , and small ions ( $\text{Al}, \text{Cr}, \text{Fe}, \text{Ti}$ ) $^{3+}$  stabilized polytypes 3O and 3T. We note the important role of pyrochlore in the structure of the 4M zirconolite polytype and the 8C polysome of

murataite, which once again confirms the close relationship between the structures of these phases. In general, EBSD is an effective method for diagnosing polytypes and members of polysomatic series in HLW crystalline matrices.

**Author Contributions:** Conceptualization, S.V.Y. and M.S.N.; methodology, M.S.N.; software, M.S.N.; validation, S.V.Y., M.S.N. and M.I.O.; formal analysis, M.I.O.; investigation, S.V.Y., M.S.N., O.I.S., B.S.N. and A.S.U.; resources, S.V.Y.; data curation, S.V.Y. and M.S.N.; writing—original draft preparation, S.V.Y., M.S.N. and M.I.O.; writing—review and editing, S.V.Y., M.S.N. and M.I.O.; visualization, M.S.N.; supervision, S.V.Y.; project administration, S.V.Y.; funding acquisition, S.V.Y. All authors have read and agreed to the published version of the manuscript.

**Funding:** This investigation was funded by the Russian Foundation for Basic Research, project “Crystal chemistry of matrices for long-lived radionuclides” No. 20-05-00058-a.

**Institutional Review Board Statement:** Not applicable.

**Informed Consent Statement:** Not applicable.

**Data Availability Statement:** All data are available within the paper.

**Acknowledgments:** Authors are thankful to anonymous reviewers for their valuable comments that improved our manuscript.

**Conflicts of Interest:** The authors declare no conflict of interest.

## Appendix A

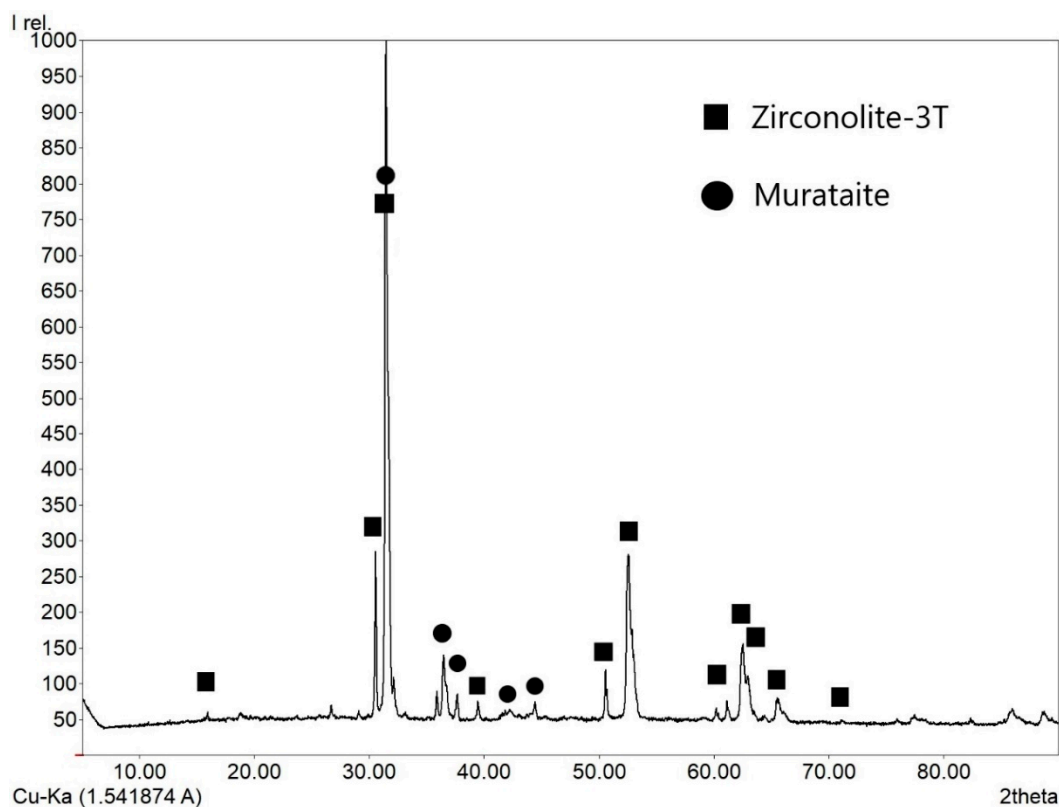


Figure A1. X-ray diffraction pattern of the sample “Th”.



## Appendix B

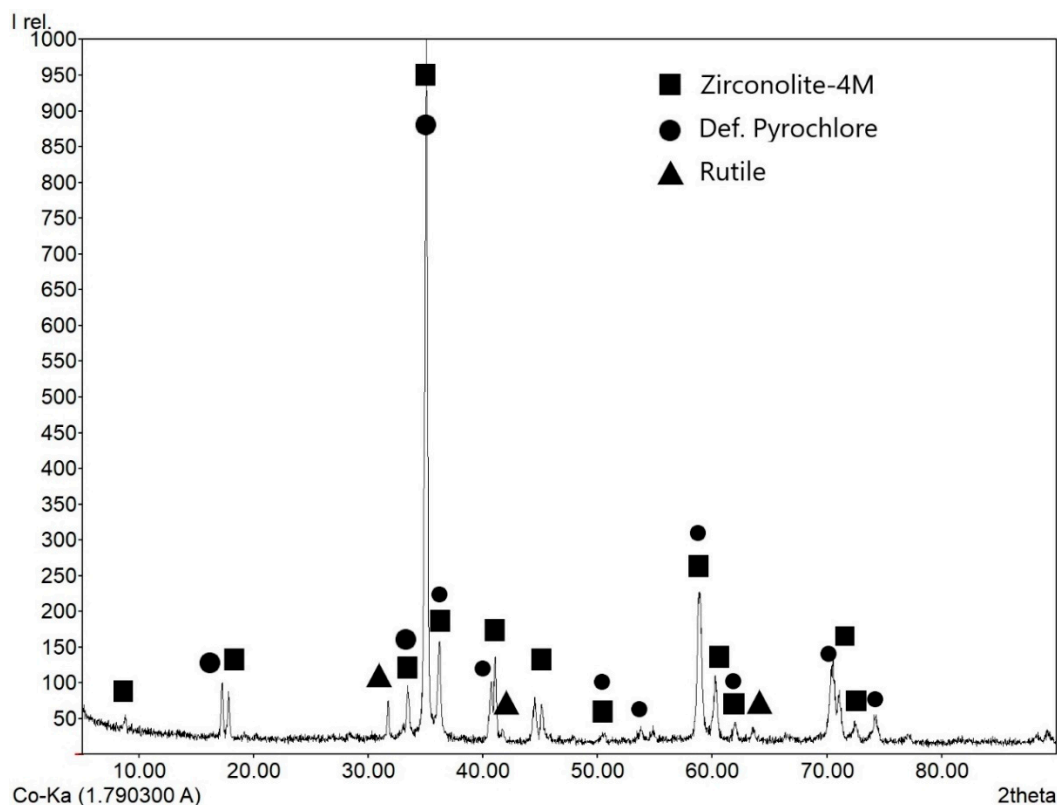


Figure A2. X-ray diffraction pattern of the sample “Nd”.

## References

- Adamov, E.O.; Mochalov, Y.S.; Rachkov, V.I.; Khomyakov, Y.S.; Shadrin, A.Y.; Kascheev, V.A.; Khaperskaya, A.V. Spent nuclear fuel reprocessing and nuclear materials recycling in two-component nuclear energy. *At. Energy* **2021**, *130*, 29–35. [[CrossRef](#)]
- Implications of Partitioning and Transmutation in Radioactive Waste Management*; Technical Reports Series, No. 435; IAEA: Vienna, Austria, 2004; 127p.
- Westlen, D. Reducing radiotoxicity in the long run. *Progr. Nucl. Energy* **2007**, *49*, 597–605. [[CrossRef](#)]
- Potential Benefits and Impacts of Advanced Nuclear Nuclear Fuel Cycles with Actinide Partitioning and Transmutation*; Rep. 6894; NEA OECD: Paris, France, 2011; 73p.
- Berthou, V.; Degueldre, C.; Magill, J. Transmutation characteristics in thermal and fast neutron spectra: Application to americium. *J. Nucl. Mater.* **2003**, *320*, 156–162. [[CrossRef](#)]
- Fuels and Materials for Transmutation*; Rep. 5419; NEA OECD: Paris, France, 2005; 239p.
- Salvatores, M.; Palmiotti, G. Radioactive waste partitioning and transmutation within advanced fuel cycles: Achievements and challenges. *Progr. Particle Nucl. Phys.* **2011**, *66*, 144–166. [[CrossRef](#)]
- Adamov, E.O.; Lopatkin, A.V.; Muravyov, E.V.; Rachkov, V.I.; Khomyakov, Y.S. National strategy for the development of nuclear energy: Two approaches to a new technological platform for nuclear energy. *Izv. RAN Energy* **2019**, 3–14. (In Russian) [[CrossRef](#)]
- Lopatkin, A.V.; Platonov, I.V.; Popov, V.E. Conditions for reaching radiation equivalence of native raw materials and long-lived radioactive waste in nuclear energy in Russia. *At. Energy* **2021**, *129*, 188–193. [[CrossRef](#)]
- Ivanov, V.K.; Chekin SYu Menyailo, A.N.; Maksyutov, M.A.; Tumanov, K.A.; Kashcheeva, P.V.; Lovachev, S.S.; Spirin, E.V.; Solomatin, V.M. Radiotoxicity of long-lived high-level waste from fast reactors in scenarios for handling irradiated nuclear fuel to achieve radiation and radiological equivalence with natural uranium. *Radiat. Risk* **2019**, *28*, 8–24. (In Russian) [[CrossRef](#)]
- Spent Nuclear Fuel Reprocessing Flowsheet*; NEA OECD: Paris, France, 2012; 120p.
- State-of-the-Art Report on the Progress of Nuclear Fuel CYCLE Chemistry*; NEA: Paris, France, 2018; 299p.
- Skupov, M.V.; Glushenkov, A.E.; Tarasov, B.A.; Abramov, S.V.; Kuzin, M.A.; Nikitin, O.N.; Zabudko, L.M.; Grachev, A.F.; Zherebtsov, A.A.; Mochalov, Y.S. Development of Technologies for Production of Fuel with Minor Actinides. *Nucl. Engin. Des.* **2021**, *382*, 111379. [[CrossRef](#)]
- Kuzin, M.A.; Abramov, S.V.; Grachev, A.F.; Zherebtsov, A.A.; Zabudko, L.M.; Nikitin, O.N.; Kuzmin, S.V. Production and study of tablets of mixed nitrides of uranium, plutonium, americium and neptunium. *Chem. Technol.* **2021**, *22*, 36–43. (In Russian)
- NEA Annual Report*; NEA OECD: Paris, France, 2021; p. 91.
- Uranium 2016: Resources, Production and Demand*; NEA OECD: Paris, France, 2016; 546p.

17. *Geological Classification of Uranium Deposits and Description of Selected Examples*; IAE: Vienna, Austria, 2018; 417p.
18. *World Uranium Geology, Exploration, Resources and Production*; IAEA: Vienna, Austria, 2020; 972p.
19. Brookins, D.G. *Geochemical Aspects of Radioactive Waste Disposal*; Springer: New York, NY, USA, 1984; 347p.
20. *Plutonium Separation in Nuclear Power Programs. Status, Problems, and Prospects of Civilian Reprocessing Around the World*; Princeton University: Princeton, NJ, USA, 2015; p. 182.
21. Ojovan, M.I.; Lee, W.E.; Kalmykov, S.N. *An Introduction to Nuclear Waste Immobilization*, 3rd ed.; Elsevier: Amsterdam, The Netherlands, 2019; p. 497.
22. Lumpkin, G.R. Alpha-decay damage and aqueous durability of actinide host phases in natural systems. *J. Nucl. Mater.* **2001**, *289*, 136–166. [[CrossRef](#)]
23. Omel'yanenko, B.I.; Livshits, T.S.; Yudintsev, S.V.; Nikonov, B.S. Natural and artificial minerals as matrices for immobilization of actinides. *Geol. Ore Depos.* **2007**, *49*, 173–193. [[CrossRef](#)]
24. Lumpkin, G.R.; Geisler-Wierwille, T. Minerals and Natural Analogues. In *Comprehensive Nuclear Materials*; Konings, R., Allen, T., Stoller, R., Yamanak, S., Eds.; Elsevier: Amsterdam, The Netherlands, 2012; pp. 563–600.
25. Lumpkin, G.R. Ceramic Host Phases for Nuclear Waste Remediation. In *Experimental and Theoretical Approaches to Actinide Chemistry*; Gibson, J.K., de Jong, W.A., Eds.; Wiley & Sons Ltd.: Hoboken, NJ, USA, 2018; pp. 333–377.
26. Wu, F.-Y.; Yang Yu Mitchell, R.H.; Bellatreccia, F.; Li, Q.-L.; Zhao, Z.-F. In situ U–Pb and Nd–Hf–(Sr) isotopic investigations of zirconolite and calzirtite. *Chem. Geol.* **2010**, *277*, 178–195. [[CrossRef](#)]
27. Apted, M.J.; Ahn, J. (Eds.) *Geological Repository Systems for Safe Disposal of Spent Nuclear Fuels and Radioactive Waste*; Woodhead Publishing Series in Energy; Elsevier: Amsterdam, The Netherlands, 2017; 778p.
28. Ringwood, A.E. Disposal of high-level nuclear wastes: A geological perspective. *Mineral. Mag.* **1985**, *49*, 159–176. [[CrossRef](#)]
29. *Scientific and Technical Basis for Geological Disposal of Radioactive Wastes*; IAE: Vienna, Austria, 2003; 80p.
30. *Management and Disposal of High-Level Radioactive Waste: Global Progress and Solutions*; NEA: Paris, France, 2020; 45p.
31. Laverov, N.P.; Yudintsev, S.V.; Kochkin, B.T.; Malkovsky, V.I. The Russian strategy of using crystalline rock as a repository for nuclear waste. *Elements* **2016**, *12*, 253–256. [[CrossRef](#)]
32. *Strategies and Considerations for the Back End of the Fuel Cycle*; NEA: Paris, France, 2021; 67p.
33. Zilberman, B.Y.; Puzikov, E.A.; Ryabkov, D.V.; Makarychev-Mikhailov, M.N.; Shadrin, A.Y.; Fedorov, Y.S.; Simonenko, V.A. Development, analysis, and simulation of a technological structure for reprocessing irradiated nuclear fuel from nuclear power plants by water-extraction methods. *At. Energy* **2009**, *107*, 333–347. [[CrossRef](#)]
34. Modolo, G.; Geist, A.; Miguirditchian, M. Minor actinide separations in the reprocessing of spent nuclear fuels: Recent advances in Europe. In *Reprocessing and Recycling of Spent Nuclear Fuel*; Elsevier: Amsterdam, The Netherlands, 2015; Volume 10, pp. 245–287.
35. Veliscek-Carolan, J. Separation of actinides from spent nuclear fuel: A review. *J. Hazard. Mater.* **2016**, *318*, 266. [[CrossRef](#)] [[PubMed](#)]
36. Baron, P.; Cornet, S.M.; Collins, E.D.; De Angelis, G.; Del Cul, G.; Fedorov Yu Glatz, J.P.; Ignatiev, V.; Inoue, T.; Khaperskaya, A.; Kim, I.T.; et al. A review of separation processes proposed for advanced fuel cycles based on technology readiness level assessments. *Progr. Nucl. Energy* **2019**, *117*, 103091. [[CrossRef](#)]
37. Ewing, R.C. Plutonium and “minor” actinides: Safe sequestration. *Earth Planet. Sci. Lett.* **2005**, *229*, 165–181. [[CrossRef](#)]
38. Ewing, R.C. The nuclear fuel cycle versus the carbon cycle. *The Canad. Mineral.* **2005**, *43*, 2099–2116. [[CrossRef](#)]
39. Frankel, G.S.; Vienna, J.D.; Lian, J.; Guo, X.; Gin, S.; Kim, S.H.; Du, J.; Ryan, J.V.; Wang, J.; Windl, W.; et al. Recent advances in corrosion science applicable to disposal of high-level nuclear waste. *Chem. Rev.* **2021**, *121*, 12327. [[CrossRef](#)]
40. Vance, E.R.; Zhang, Y.; Gregg, D.J. Ceramic Waste Forms. In *Comprehensive Nuclear Materials*, 2nd ed.; Konings, R., Stoller, R., Eds.; Elsevier: Amsterdam, The Netherlands, 2020; Volume 6, pp. 445–466.
41. Ewing, R.C.; Weber, W.J. Actinide waste forms and radiation effects. In *Actinide and Transactinide Elements*; Morss, L.R., Edelstein, N.M., Fuger, J., Eds.; Springer: Dordrecht, The Netherlands, 2010; Volume 6, pp. 3813–3887.
42. National Research Council. *Waste Forms Technology and Performance: Final Report*; National Academies Press: Washington, DC, USA, 2011; p. 308.
43. Hyatt, N.C.; Ojovan, M.I. Materials for Nuclear Waste Immobilization. *Materials* **2019**, *12*, 3611. [[CrossRef](#)] [[PubMed](#)]
44. Blackburn, L.R.; Bailey, D.J.; Sun, S.-K.; Gardner, L.J.; Stennett, M.C.; Corkhill, C.L.; Hyatt, N.C. Review of zirconolite crystal chemistry and aqueous durability. *Adv. Appl. Ceram.* **2021**, *120*, 69–83. [[CrossRef](#)]
45. *High Level Solidified Waste. General Technical Requirements*; GOST R-50926-96; Gosstandart of Russia: Moscow, Russia, 1996. (In Russian)
46. Poluektov, P.P.; Sukhanov, L.P.; Matyunin, Y.I. Scientific approaches and technical solutions in the field of high-level liquid waste management. *Russ. Chem. Mag.* **2005**, *49*, 29–41. (In Russian)
47. Gumber, N.; Pai, R.V.; Phatak, R.; Adiraju, B.; Sahu, M.; Jagannath, J.; Sudarshan, K. Synthesis, characterization and crystal chemistry of uranium and cerium doped yttrium titanate pyrochlore: A potential waste immobilization matrix. *J. Nucl. Mater.* **2021**, *556*, 153191. [[CrossRef](#)]
48. Yudintsev, S.V. Lanthanide titanates as promising matrices for immobilization of actinide wastes. *Dokl. Earth Sci.* **2015**, *460*, 130–136. [[CrossRef](#)]
49. Yudintsev, S.V. Isolation of separated waste of nuclear industry. *Radiochemistry* **2021**, *63*, 527. [[CrossRef](#)]

50. Shannon, R.D. Revised effective ionic radii and systematic studies of interatomic distances in halides and chalcogenides. *Acta Crystallogr. Sect. A* **1976**, *32*, 751–767. [[CrossRef](#)]
51. Fielding, P.E.; White, T.J. Crystal chemical incorporation of high-level waste species in aluminotitanate-based ceramics: Valence, location, radiation damage, and hydrothermal durability. *J. Mater. Res.* **1987**, *2*, 387–414. [[CrossRef](#)]
52. Yudinsev, S.V. A structural–chemical approach to selecting crystalline matrices for actinide immobilization. *Geol. Ore Deposits*. **2003**, *45*, 151–165.
53. Orlova, A.I.; Orlova, V.A.; Orlova, M.P.; Bykov, D.M.; Stefanovskii, S.V.; Stefanovskaya, O.I.; Nikonov, B.S. The crystal-chemical principle in designing mineral-like phosphate ceramics for immobilization of radioactive waste. *Radiochemistry* **2006**, *48*, 330–339. [[CrossRef](#)]
54. Orlova, A.I. Development of mineral-like materials based on phosphates and complex oxides for HLW immobilization. Crystal chemical concept. *Probl. Radiat. Saf.* **2015**, *3*, 67–76. (In Russian)
55. Orlova, A.; Chuvildeev, V. Chemistry, crystal chemistry and SPS technology for elaboration of perspective materials for nuclear wastes and minor actinides consolidation. *J. Nucl. Med. Radiat. Ther.* **2016**, *7*, 36.
56. Orlova, A.I.; Ojovan, M.I. Ceramic Mineral Waste-Forms for Nuclear Waste Immobilization. *Materials* **2019**, *12*, 2638. [[CrossRef](#)] [[PubMed](#)]
57. Zhang, Y.; Kong, L.; Ionescu, M.; Gregg, D.J. Current advances on titanate glass-ceramic composite materials as waste forms for actinide immobilization: A technical review. *J. Eur. Ceram. Soc.* **2022**, *42*, 1852–1876. [[CrossRef](#)]
58. Gin, S.; Jollivet, P.; Tribet, M.; Peugeot, S.; Schuller, S. Radionuclides containment in nuclear glasses: An overview. *Radiochimica Acta*. **2017**, *105*, 927–959. [[CrossRef](#)]
59. Yang, K.; Lei, P.; Yao, T.; Gong, B.; Wang, Y.; Li, M.; Wang, J.; Lian, J. A systematic study of lanthanide titanates ( $A_2Ti_2O_7$ ) chemical durability: Corrosion mechanisms and control parameters. *Corros. Sci.* **2021**, *185*, 109394. [[CrossRef](#)]
60. Yang, K.; Wang, Y.; Lei, P.; Yao, T.; Zhao, D.; Lian, J. Chemical durability and surface alteration of lanthanide zirconates ( $A_2Zr_2O_7$ : A = La–Yb). *J. Eur. Ceram. Soc.* **2021**, *41*, 6018–6028. [[CrossRef](#)]
61. Gong, B.; Yang, K.; Lian, J.A.; Wang, J. Machine learning-enabled prediction of chemical durability of  $A_2B_2O_7$  pyrochlore and fluorite. *Comput. Mater. Sci.* **2021**, *200*, 110820. [[CrossRef](#)]
62. Babelot, C. Monazite-type ceramics for conditioning of minor actinides: Structural characterization and properties. *Reihe Energ. Umw. Energy Environ.* **2012**, *182*, 129.
63. Ramsdell, L.S. Studies on silicon carbide. *Am. Mineral.* **1947**, *32*, 64–71.
64. Thompson, J.B. Biopyriboles and polysomatic series. *Am. Mineral.* **1978**, *63*, 239–249.
65. Veblen, D.R. Polysomatism and polysomatic series: A review and applications. *Am. Mineral.* **1991**, *76*, 801–826.
66. Laverov, N.P.; Urusov, V.S.; Krivovichev, S.V.; Pakhomova, A.S.; Stefanovsky, S.V.; Yudinsev, S.V. Modular nature of the polysomatic pyrochlore–murataite series. *Geol. Ore Depos.* **2011**, *53*, 273–294. [[CrossRef](#)]
67. Laverov, N.P.; Yudinsev, S.V.; Stefanovskii, S.V.; Omel’yanenko, B.I.; Nikonov, B.S. Murataite Matrices for Actinide Wastes. *Radiochemistry* **2011**, *53*, 229–243. [[CrossRef](#)]
68. Pakhomova, A.S.; Krivovichev, S.V.; Yudinsev, S.V.; Stefanovsky, S.V. Polysomatism and structural complexity: Structure model for murataite-8C, a complex crystalline matrix for the immobilization of high-level radioactive waste. *Eur. J. Mineral.* **2016**, *28*, 205–214. [[CrossRef](#)]
69. Ewing, R.C. Actinides and radiation effects: Impact on the back-end of the nuclear fuel cycle. *Mineral. Mag.* **2011**, *75*, 2359–2377. [[CrossRef](#)]
70. Zhang, K.; Luo, B.; Zhang, H. Immobilization of  $CeO_2$  using single-phase zirconolite and the chemical stability analysis. *Mater. Res. Express* **2019**, *6*, 115526. [[CrossRef](#)]
71. Zhang, S.; Xu, B.; Cheng, J.; Luo, S.; Ding, Y.; Ji, S.; Duan, T.; Ma, J.; Jiang, C. Phase evolution and chemical stability of Nd-doped  $Y_3Fe_5O_{12}$  waste forms synthesized in molten salt at a low temperature. *J. Am. Ceram. Soc.* **2021**, *105*, 1459–1471. [[CrossRef](#)]
72. Ringwood, A.E.; Kesson, S.E.; Ware, N.G.; Hibberson, W.O.; Major, A. The SYNROC process: A geochemical approach to nuclear waste immobilization. *Geochem. J.* **1979**, *13*, 141–169. [[CrossRef](#)]
73. Ringwood, A.E.; Kesson, S.E.; Ware, N.G.; Hibberson, W.O.; Major, A. Immobilisation of high-level nuclear reactor wastes in SYNROC. *Nature* **1979**, *278*, 219–223. [[CrossRef](#)]
74. Ringwood, A.E.; Kesson, S.E.; Reeve, K.D.; Levins, D.M.; Ramm, E.J. Synroc. In *Radioactive Waste Forms for the Future*; Lutze, W., Ewing, R.C., Eds.; Elsevier: New York, NY, USA, 1988; pp. 233–334.
75. Laverov, N.P.; Omel’yanenko, B.I.; Yudinsev, S.V.; Nikonov, B.S. Zirconolite as a matrix for immobilization of high-level radioactive wastes (HLW). *Geol. Ore Depos.* **1996**, *38*, 345–352.
76. Advocat, T.; Fillet, C.; Marillet, J.; Boubals, J.M.; Bonnetier, A. Nd-doped zirconolite ceramic and glass ceramic synthesized by melting and controlled cooling. *Mat. Res. Soc. Symp. Proc.* **1998**, *506*, 55–61. [[CrossRef](#)]
77. Advocat, T.; McGlinn, P.J.; Fillet, C.; Leturcq, G.; Schuller, S.; Bonnetier, A.; Hart, K. Melted synthetic zirconolite-based matrices: Effect of cooling rate and heat treatment on ceramic microstructure and chemical durability. *Mat. Res. Soc. Symp. Proc.* **2001**, *663*, 277–284. [[CrossRef](#)]
78. Xu, H.; Wang, Y. Crystallization sequence and microstructure evolution of Synroc samples crystallized from  $CaZrTi_2O_7$  melts. *J. Nucl. Mater.* **2000**, *279*, 100–106. [[CrossRef](#)]

79. Vance, E.R.; Lumpkin, G.R.; Carter, M.L.; Cassidy, D.J.; Ball, C.J.; Day, R.A.; Begg, B.D. Incorporation of Uranium in Zirconolite ( $\text{CaZrTi}_2\text{O}_7$ ). *J. Am. Ceram. Soc.* **2002**, *85*, 1853–1859. [CrossRef]
80. Loiseau, P.; Caurant, D.; Baffier, N.; Mazerolles, L.; Fillet, C. Glass–ceramic nuclear waste forms obtained from  $\text{SiO}_2$ – $\text{Al}_2\text{O}_3$ – $\text{CaO}$ – $\text{ZrO}_2$ – $\text{TiO}_2$  glasses containing lanthanides (Ce, Nd, Eu, Gd, Yb) and actinides (Th): Study of internal crystallization. *J. Nucl. Mater.* **2004**, *335*, 14–32. [CrossRef]
81. Vance, E.R.; Moricca, S.; Begg, B.D.; Stewart, M.W.A.; Zhang, Y.; Carter, M.L. Advantages hot isostatically pressed ceramic and glass-ceramic waste forms bring to the immobilization of challenging intermediate- and high-level nuclear wastes. *Adv. Sci. Technol.* **2010**, *73*, 130–135.
82. Stefanovsky, S.V.; Chizhevskaya, S.V.; Mironov, A.S.; Kiryanova, O.I.; Yudin, S.V. Synthetic calcium-free REE-substituted zirconolites. *Perspekt. Mater.* **2003**, *6*, 61–68. (In Russian)
83. Strachan, D.M.; Scheele, R.D.; Buck, E.C.; Kozelisky, A.E.; Sell, R.L.; Elovich, R.J.; Buchmiller, W.C. Radiation damage effects in candidate titanates for Pu disposition: Zirconolite. *J. Nucl. Mater.* **2008**, *372*, 16–31. [CrossRef]
84. Yin, D.; Zhang, K.; Peng, L.; He, Z.; Liu, Y.; Zhang, H.; Lu, X. Solid-state reaction synthesis and chemical stability studies in Nd-doped zirconolite-rich ceramics. *J. Rare Earths.* **2018**, *36*, 492–498. [CrossRef]
85. Zhang, K.; Yin, D.; Lu, X.; Zhang, H. Self-propagating high-temperature synthesis, phase composition and aqueous durability of Nd–Al bearing zirconolite-rich composites as nuclear waste form. *Adv. Appl. Ceram.* **2018**, *117*, 78–84. [CrossRef]
86. Blackburn, L.R.; Gardner, L.J.; Sun, S.K.; Maddrell, E.R.; Stennett, M.C.; Corkhill, C.L.; Hyatt, N.C. Hot Isostatically Pressed Zirconolite Wasteforms for Actinide Immobilisation. *IOP Conf. Ser. Mater. Sci. Eng.* **2020**, *818*, 012010. [CrossRef]
87. Gregg, D.J.; Farzana, R.; Dayal, P.; Holmes, R.; Triani, G. Synroc technology: Perspectives and current status (Review). *J. Am. Ceram. Soc.* **2020**, *103*, 5424–5441. [CrossRef]
88. Zhu, H.; Wang, F.; Liao, Q.; Zhu, Y. Synthesis and characterization of zirconolite–sodium borosilicate glass-ceramics for nuclear waste immobilization. *J. Nucl. Mater.* **2020**, *532*, 152026. [CrossRef]
89. Zhu, H.; Wang, F.; Liao, Q.; Wang, Y.; Zhu, Y. Effect of  $\text{CeO}_2$  and  $\text{Nd}_2\text{O}_3$  on phases, microstructure and aqueous chemical durability of borosilicate glass-ceramics for nuclear waste immobilization. *Mater. Chem. Phys.* **2020**, *249*, 122936. [CrossRef]
90. Caurant, D.; Majérus, O. Glasses and Glass-Ceramics for Nuclear Waste Immobilization. In *Encyclopedia of Materials: Technical Ceramics and Glasses*; Pomeroy, M., Ed.; Elsevier: Oxford, UK, 2021; Volume 2, pp. 762–790.
91. Aldean, I.; Sun, S.-K.; Wilkins, M.C.D.; Gardner, L.J.; Mason, A.R.; Stennett, M.C.; Corkhill, C.L.; Hyatt, N.C.; Blackburn, L.R. Synthesis and characterisation of Ce-doped zirconolite  $\text{Ca}_{0.80}\text{Ce}_{0.20}\text{ZrTi}_{1.60}\text{M}_{0.40}\text{O}_7$  ( $\text{M} = \text{Fe}, \text{Al}$ ) formed by reactive spark plasma sintering (RSPS). *Mat. Res. Soc. Adv.* **2022**, *7*, 75–80. [CrossRef]
92. Dayal, P.; Farzana, R.; Zhang, Y.; Lumpkin, G.R.; Holmes, R.; Triani, G.; Gregg, D.J. Profiling hot isostatically pressed canister–wasteform interaction for Pu-bearing zirconolite-rich wasteforms. *J. Am. Ceram. Soc.* **2022**, *105*, 1–14. [CrossRef]
93. Williams, C.T.; Giere, R. Zirconolite: A Review of localities worldwide, and a compilation of its chemical compositions. *Bull. Nat. Hist. Mus. Lond.* **1996**, *52*, 1–24.
94. Hudson Institute of Mineralogy. mindat.org. Zirconolite. Available online: <https://www.mindat.org/min-4422.html> (accessed on 6 July 2022).
95. Bayliss, P.; Mazzi, F.; Munno, R.; White, T.J. Mineral nomenclature: Zirconolite. *Mineral. Mag.* **1989**, *53*, 565–569. [CrossRef]
96. Ventura, G.D.; Bellatreccia, F.; Williams, T. Zirconolite with significant REE $\text{ZrNb}(\text{Mn}, \text{Fe})\text{O}_7$  from a xenolith of the Laacher see eruptive center, Eifel volcanic region, Germany. *The Canad. Mineral.* **2000**, *38*, 57–65. [CrossRef]
97. Zubkova, N.V.; Chukanov, N.V.; Pekov, I.V.; Ternes, B.; Schüller, W.; Ksenofontov, D.A.; Pushcharovsky, D.Y. The crystal structure of nonmetamict Nb-rich zirconolite-3T from the Eifel paleovolcanic region, Germany. *Z. Krist.* **2018**, *233*, 463–468. [CrossRef]
98. Kesson, S.E.; Sinclair, W.J.; Ringwood, A.E. Solid solution limits in Synroc zirconolite. *Nucl. Chem. Waste Managem.* **1983**, *4*, 259–265.
99. Coelho, A.A.; Cheary, R.W.; Smith, K.L. Analysis and structural determination of Nd-substituted zirconolite-4M. *J. Solid State Chem.* **1997**, *129*, 346–359. [CrossRef]
100. Caurant, D.; Loiseau, P.; Bardez, I. Structural characterization of Nd-doped Hf-zirconolite  $\text{Ca}_{1-x}\text{Nd}_x\text{HfTi}_{2-x}\text{Al}_x\text{O}_7$  ceramics. *J. Nucl. Mater.* **2010**, *407*, 88–99. [CrossRef]
101. Mazzi, F.; Munno, R. Calciobetafite (new mineral of the pyrochlore group) and related minerals from Campi Flegrei, Italy; crystal structures of polymignyte and zirkelite: Comparison with pyrochlore and zirconolite. *Am. Mineral.* **1983**, *68*, 262–276.
102. White, T.J. The microstructure and microchemistry of synthetic zirconolite, zirkelite and related phases. *Am. Mineral.* **1984**, *69*, 1156–1172.
103. Smith, K.L.; Lumpkin, G.R. Structural features of zirconolite, hollandite and perovskite, the major waste-bearing phases in Synroc. In *Defects and Processes in the Solid State: Geoscience Applications*; Boland, J.N., Fitzgerald, J.D., Eds.; Elsevier: Amsterdam, The Netherlands, 1993; pp. 401–422.
104. Blackburn, L.R.; Sun, S.-K.; Gardner, L.J.; Maddrell, E.R.; Stennett, M.C.; Corkhill, C.L.; Hyatt, N.C. Synthesis, structure, and characterization of the thorium zirconolite  $\text{CaZr}_{1-x}\text{Th}_x\text{Ti}_2\text{O}_7$  system. *J. Am. Ceram. Soc.* **2021**, *104*, 2937–2951. [CrossRef]
105. Gilbert, M.R.; Selfslag, C.; Walter, M.; Stennett, M.C.; Somers, J.; Hyatt, N.C.; Livens, F.R. Synthesis and characterisation of Pu-doped zirconolites— $(\text{Ca}_{1-x}\text{Pu}_x)\text{Zr}(\text{Ti}_{2-2x}\text{Fe}_{2x})\text{O}_7$ . *IOP Conf. Ser. Mater. Sci. Eng.* **2009**, *9*, 012007. [CrossRef]
106. Grey, I.E.; Mumme, W.G.; Ness, T.J.; Roth, R.S.; Smith, K.L. Structural relations between weberite and zirconolite polytypes—Refinements of doped 3T and 4M  $\text{Ca}_2\text{Ta}_2\text{O}_7$  and 3T  $\text{CaZrTi}_2\text{O}_7$ . *J. Solid State Chem.* **2003**, *174*, 285–295. [CrossRef]



107. Kong, L.; Karatchevtseva, I.; Zhang, Y.; Wei, T. The incorporation of Nd or Ce in CaZrTi<sub>2</sub>O<sub>7</sub> zirconolite: Ceramic versus glass-ceramic. *J. Nucl. Mater.* **2021**, *543*, 152583. [[CrossRef](#)]
108. Cachia, J.-N.; Deschanel, X.; Auwer, C.D.; Pinet, O.; Phalippou, J.; Hennig, C.; Scheinost, A. Enhancing cerium and plutonium solubility by reduction in borosilicate glass. *J. Nucl. Mater.* **2006**, *352*, 182–189. [[CrossRef](#)]
109. Caurant, D.; Majerus, O.; Loiseau, P.; Bardez, I.; Baffier, N.; Dussossoy, J.L. Crystallization of neodymium-rich phases in silicate glasses developed for nuclear waste immobilization. *J. Nucl. Mater.* **2006**, *354*, 143–162. [[CrossRef](#)]
110. McCloy, J.S.; Schuller, S. Vitrification of wastes: From unwanted to controlled crystallization, a review. *Comptes Rendus. Géoscience* **2022**, *354*, 1–40. [[CrossRef](#)]
111. Blackburn, L.R.; Sun, S.; Gardner, L.J.; Maddrell, E.R.; Stennet, M.C.; Hyatt, N.C. A systematic investigation of the phase assemblage and microstructure of the zirconolite CaZr<sub>1-x</sub>Ce<sub>x</sub>Ti<sub>2</sub>O<sub>7</sub>. *J. Nucl. Mater.* **2020**, *535*, 152137. [[CrossRef](#)]
112. Ji, S.; Su, M.; Liao, C.; Ma, S.; Wang, Z.; Shih, K.; Chang, C.-K.; Lee, J.-F.; Chan, T.-S.; Li, Y. Synchrotron x-ray spectroscopy investigation of the Ca<sub>1-x</sub>Ln<sub>x</sub>ZrTi<sub>2-x</sub>(Al,Fe)<sub>x</sub>O<sub>7</sub> zirconolite ceramics (Ln = La, Nd, Gd, Ho, Yb). *J. Am. Ceram. Soc.* **2020**, *103*, 1463–1475. [[CrossRef](#)]
113. Maddrell, E.R.; Paterson, H.C.; May, S.E.; Burns, K.M. Phase evolution in zirconolite glass-ceramic wasteforms. *J. Nucl. Mater.* **2017**, *423*, 380–387. [[CrossRef](#)]
114. Vance, E.R.; Agraval, D.K. Incorporation of radionuclides in crystalline titanates. *Nucl. Chem. Waste Managem.* **1982**, *3*, 229–234. [[CrossRef](#)]
115. Weber, W.J.; Ewing, R.C.; Catlow, C.R.A. Radiation effects in crystalline ceramics for the immobilization of high-level nuclear waste and plutonium. *J. Mat. Res.* **1998**, *13*, 1434–1479. [[CrossRef](#)]
116. Zhang, Y.; Stewart, M.W.A.; Li, H.; Carter, M.L.; Vance, E.R.; Moricca, S. Zirconolite-rich titanate ceramics for immobilisation of actinides—Waste form/HIP can interactions and chemical durability. *J. Nucl. Mater.* **2009**, *395*, 69–74. [[CrossRef](#)]
117. Amoroso, J.; Marra, J.C.; Tang, M.; Lin, Y.; Chen, F.; Su, D.; Brinkman, K.S. Melt processed multiphase ceramic waste forms for nuclear waste immobilization. *J. Nucl. Mater.* **2014**, *454*, 12–21. [[CrossRef](#)]
118. Leturcq, G.; McGlenn, P.J.; Barbe, C.; Blackford, M.G.; Finnie, K.S. Aqueous alteration of nearly pure Nd-doped zirconolite (Ca<sub>0.8</sub>Nd<sub>0.2</sub>ZrTi<sub>1.8</sub>Al<sub>0.2</sub>O<sub>7</sub>), a passivating layer control. *Appl. Geochem.* **2005**, *20*, 899–906. [[CrossRef](#)]
119. Pöml, P.; Geisler, T.; Cobos-Sabaté, J.; Wiss, T.; Raison, P.E.; Schmid-Beurmann, P.; Deschanel, X.; Jégou, C.; Heimink, J.; Putnis, A. The mechanism of the hydrothermal alteration of cerium- and plutonium-doped zirconolite. *J. Nucl. Mater.* **2011**, *410*, 10–23. [[CrossRef](#)]
120. Jafar, M.; Sengupta, P.; Achary, S.N.; Tyagi, A.K. Phase evolution and microstructural studies in CaZrTi<sub>2</sub>O<sub>7</sub> (zirconolite)—Sm<sub>2</sub>Ti<sub>2</sub>O<sub>7</sub> (pyrochlore) system. *J. Eur. Ceram. Soc.* **2014**, *34*, 4373–4381. [[CrossRef](#)]
121. Malmström, J.; Reusser, E.; Gieré, R.; Lumpkin, G.R.; Düggelin, M.; Mathys, D.; Guggenheim, R. Zirconolite corrosion in dulite acidic and basic fluids at 180–700 °C and 50 MPa. *Mat. Res. Soc. Symp. Proc.* **1999**, *556*, 165–172. [[CrossRef](#)]
122. Malmstrom, J.; Reusser, E.; Giere, R.; Lumpkin, G.R.; Blackford, M.G.; Düggelin, M.; Mathys, D.; Guggenheim, R.; Gunther, D. Formation of perovskite and calzirtite during zirconolite alteration. *Mat. Res. Soc. Symp. Proc.* **2000**, *608*, 475–480. [[CrossRef](#)]
123. Bakel, A.J.; Mertz, C.J.; Hash, M.C.; Chamberlain, D.B. The long-term corrosion behavior of titanate ceramics for Pu disposition: Rate-controlling processes. *Mat. Res. Soc. Symp. Proc.* **2000**, *608*, 387–392. [[CrossRef](#)]
124. Gieré, R.; Malmström, J.; Reusser, E.; Lumpkin, G.R.; Düggelin, M.; Mathys, D.; Guggenheim, R.; Günther, D. Durability of zirconolite in hydrothermal fluids: Implications for nuclear waste disposal. *Mat. Res. Soc. Symp. Proc.* **2001**, *663*, 267–276. [[CrossRef](#)]
125. Morgan, P.E.D.; Ryerson, F.J. A new “cubic” crystal compound. *J. Mater. Sci. Lett.* **1982**, *1*, 351–352. [[CrossRef](#)]
126. Laverov, N.P.; Yudinsev, S.V.; Stefanovsky, S.V.; Omel’yanenko, B.I.; Nikonov, B.S. Murataite as a universal matrix for immobilization of actinides. *Geol. Ore Depos.* **2006**, *48*, 335–356. [[CrossRef](#)]
127. Laverov, N.P.; Omel’yanenko, B.I.; Yudinsev, S.V.; Nikonov, B.S.; Sobolev, I.A.; Stefanovsky, S.V. Mineralogy and geochemistry of matrices for the immobilization of high-level radioactive wastes. *Geol. Ore Deposits.* **1997**, *39*, 179–193.
128. Yudinsev, S.V.; Danilov, S.S.; Vinokurov, S.E.; Stefanovskaya, O.I.; Nikonov, B.S.; Nikol’sky, M.S.; Skvortsov, M.V.; Myasoedov, B.F. Phase composition and hydrothermal stability of ceramics based on murataite. *Radiochemistry* **2020**, *62*, 744–751. [[CrossRef](#)]
129. Pakhomova, A.S.; Krivovichev, S.V.; Yudinsev, S.V.; Stefanovsky, S.V. Synthetic murataite-3C, a complex form for long-term immobilization of nuclear waste: Crystal structure and its comparison with natural analogues. *Z. Krist. Cryst. Mater.* **2013**, *228*, 151–156. [[CrossRef](#)]
130. Krivovichev, S.V.; Yudinsev, S.V.; Stefanovsky, S.V.; Organova, N.I.; Karimova, O.V.; Urusov, V.S. Murataite–pyrochlore series: A family of complex oxides with nanoscale pyrochlore clusters. *Angew. Chem.* **2010**, *122*, 10178–10180. [[CrossRef](#)]
131. Krivovichev, S.; Yudinsev, S.; Pakhomova, A.; Stefanovsky, S. Murataite-Pyrochlore Ceramics as Complex Matrices for Radioactive Waste Immobilization: Structural and Microstructural Mechanisms of Crystallization. In *International Congress on Applied Mineralogy*; Springer: Cham, Switzerland, 2019; pp. 447–450.
132. Yudinsev, S.; Stefanovsky, S.; Nikonov, B.; Stefanovsky, O.; Nickolskii, M.; Skvortsov, M. Phase formation at synthesis of murataite-crichtonite ceramics. *J. Nucl. Mater.* **2019**, *517*, 371–379. [[CrossRef](#)]
133. Nickolsky, M.S.; Yudinsev, S.V. Electron backscattered diffraction for the study of matrices for immobilization of actinides composed of the murataite-type phases. *Crystallogr. Rep.* **2021**, *66*, 130–141. [[CrossRef](#)]

134. Yudintsev, S.V.; Nickolsky, M.S.; Nikonov, B.S. Study of Matrices for Immobilization of  $^{99}\text{Tc}$  by the EBSD Method. *Dokl. Earth Sci.* **2021**, *500*, 794–801. [[CrossRef](#)]
135. Kikuchi, S. Diffraction of cathode rays by mica. *Proc. Imp. Acad.* **1928**, *4*, 271–274. [[CrossRef](#)]
136. Venables, J.A.; Harland, C.J. Electron back-scattering patterns—A new technique for obtaining crystallographic information in the scanning electron microscope. *Philos. Mag.* **1973**, *27*, 1193–1200. [[CrossRef](#)]
137. Schwartz, A.J.; Kumar, M.; Adamas, B.L.; Field, D.P. (Eds.) *Electron Backscatter Diffraction in Materials Science*; Springer: New York, NY, USA, 2009; p. 403.
138. Smith, C.A.; Biswas, S.; Miller, B.D.; Kombaiyah, B.; Frazer, D.; Keiser, D.D.; Aitkaliyeva, A. High burnup structure formation in U-Mo fuels. *J. Nucl. Mater.* **2022**, *563*, 153617. [[CrossRef](#)]
139. Iltis, X.; Zacharie-Aubrun, I.; Ryu, H.J.; Park, J.M.; Leenaers, A.; Yacout, A.M.; Tarisien, N. Microstructure of as atomized and annealed U-Mo<sub>7</sub> particles: A SEM/EBSD study of grain growth. *J. Nucl. Mater.* **2017**, *495*, 249–266. [[CrossRef](#)]
140. Jadernas, D.; Gan, J.; Keiser, D.; Madden, J.; Bachhav, M.; Jue, J.F.; Robinson, A. Microstructural characterization of as-fabricated and irradiated U-Mo fuel using SEM/EBSD. *J. Nucl. Mater.* **2018**, *509*, 1–8. [[CrossRef](#)]
141. Tumurugoti, P.; Clark, B.M.; Edwards, D.J.; Amoroso, J.; Sundaram, S.K. Cesium incorporation in hollandite-rich multiphasic ceramic waste forms. *J. Solid State Chem.* **2017**, *246*, 107–112. [[CrossRef](#)]
142. Peterson, J.A.; Crum, J.V.; Riley, B.J.; Asmussen, R.M.; Neeway, J.J. Synthesis and characterization of oxyapatite [ $\text{Ca}_2\text{Nd}_8(\text{SiO}_4)_6\text{O}_2$ ] and mixed-alkaline-earth powellite [(Ca,Sr,Ba)MoO<sub>4</sub>] for a glass-ceramic waste form. *J. Nucl. Mater.* **2018**, *510*, 623–634. [[CrossRef](#)]
143. Shoup, S.S.; Bamberger, C.E.; Tyree, J.L.; Anovitz, L. Lanthanide-containing zirconotitanate solid solutions. *J. Solid State Chem.* **1996**, *127*, 231–239. [[CrossRef](#)]
144. Yudintsev, S.V.; Stefanovsky, S.V.; Kalenova MYu Nikonov, B.S.; Nikol'skii, M.S.; Koshcheev, A.M.; Shchepin, A.S. Matrices for immobilization of the rare earth–actinide waste fraction, synthesized by cold crucible induction melting. *Radiochemistry* **2015**, *57*, 321–333. [[CrossRef](#)]
145. Yudintsev, S.V.; Stefanovsky, S.V.; Stefanovskaya, O.I.; Nikonov, B.S.; Nikol'skii, M.S. Phase distribution of uranium in matrices for immobilization of the rare earth–actinide fraction of high-level waste. *Radiochemistry* **2015**, *57*, 640–651. [[CrossRef](#)]
146. Yudintsev, S.V.; Livshits, T.S.; Zhang, J.; Ewing, R.C. The behavior of rare-earth pyrochlores and perovskites under ion irradiation. *Dokl. Earth Sci.* **2015**, *461*, 247–253. [[CrossRef](#)]
147. Nikolsky, M.S. Crystal Chemistry of Compounds of Rare Earth Elements with Pyrochlore Structure. Ph.D. Thesis, Moscow, Russia, 2018.
148. Yudintsev, S.V.; Nikolskii, M.S.; Nikonov, B.S.; Malkovskii, V.I. Matrices for isolation of actinide wastes in a deep well repository. *Dokl. Earth Sci.* **2018**, *480*, 631–636. [[CrossRef](#)]
149. Shoup, S.S.; Bamberger, C.E. On the formation of americium and neptunium-containing titanates. *Radiochim. Acta* **1997**, *76*, 63–69. [[CrossRef](#)]
150. Blackburn, L.R.; Townsend, L.T.; Lawson, S.M.; Mason, A.R.; Stennett, M.C.; Sun, S.-K.; Gardner, L.J.; Maddrell, E.R.; Corkhill, C.L.; Hyatt, N.C. Phase Evolution in the CaZrTi<sub>2</sub>O<sub>7</sub>–Dy<sub>2</sub>Ti<sub>2</sub>O<sub>7</sub> System: A Potential Host Phase for Minor Actinide Immobilization. *Inorg. Chem.* **2022**, *61*, 5744–5756. [[CrossRef](#)]